ELSEVIER

#### Contents lists available at ScienceDirect

# Chemical Geology

journal homepage: www.elsevier.com/locate/chemgeo





# Connecting visual metamictization to radiation damage to expand applications of zircon (U-Th)/He thermochronometry

Emma M. Armstrong<sup>a,\*</sup>, Alexis K. Ault<sup>a</sup>, Jenna M. Kaempfer<sup>a</sup>, William R. Guenthner<sup>b</sup>

#### ARTICLE INFO

Editor: Marco Fiorentini

Keywords: zircon (U-Th)/He thermochronometry Radiation damage Visual metamictization Alpha dose Raman spectroscopy

#### ABSTRACT

Zircon (U-Th)/He (ZHe) thermochronometry quantifies the timing and tempo of low-temperature processes and is used to deconvolve tectonic and erosional histories. Accumulation and annealing of radiation damage impacts He diffusion in zircon and resulting ZHe dates. Resolving complex histories requires building relationships between ZHe date, effective U (eU), and radiation damage in grains sharing a common thermal history. Prior work demonstrated that purposefully selecting grains with a spectrum of visual metamictization yields a broad range of intrasample eU values (Ault et al., 2018), but it remained unclear if visual metamictization tracks effective radiation damage. Here we evaluate relationships between visual metamictization, effective damage calculated from Raman spectroscopy, and ZHe dates from a new suite of grains from some of the same Precambrian samples investigated in Ault et al. (2018) and Phanerozoic detrital grains from Armstrong et al. (2022). New ZHe analyses (n = 21) confirm increasing visual metamictization corresponds with increasing eU concentration and dates fall along previously reported ZHe date-eU trends for each sample, despite grain selection by different analysts in different sessions. Raman-based alpha dose calculations from multiple spot analyses from transects across the surface and interior of each grain (n = 480 total analyses) range from  $3.19 \times 10^{16}$  to  $1.52 \times 10^{19}$   $\alpha/g$  across the whole dataset. Alpha dose increases in samples characterized by a clear increase in visual metamictization from different types of ZHe date-eU patterns, supporting that visual metamictization reflects effective radiation damage in these samples. Complexities in visual metamictization-damage trends are due to damage zonation observed in cathodoluminescence, comparative internal and external spot analyses, and 2-D Raman maps, as well as limited spread in intrasample visual metamictization and user grain selection bias. Overall, visual metamictization provides a qualitative estimate of effective damage and should be leveraged when selecting grains for traditional ZHe analyses to build ZHe date-eU-damage patterns.

#### 1. Introduction

Zircon (U-Th)/He (ZHe) thermochronometry is a fundamental tool for reconstructing the timing and rates of temperature-sensitive, upper crustal (~2–8 km) geologic processes (Reiners, 2005; Ault et al., 2019 and references therein). This technique exploits radioactive decay of isotopes of primarily U and Th, associated alpha particle (<sup>4</sup>He) production, and temperature-dependent <sup>4</sup>He diffusion (Reiners et al., 2004). The recognition and evolving understanding of the role of radiation damage accumulation and annealing on <sup>4</sup>He diffusion in zircon has enabled expanded applications of ZHe thermochronometry to increasingly complicated thermal histories (Guenthner et al., 2013; Ginster et al., 2019). For example, recently, zircon damage-diffusivity

relationships have been leveraged to reconstruct deep-time thermal histories in ancient rocks (e.g., DeLucia et al., 2018; Flowers et al., 2020; Peak et al., 2021; Thurston et al., 2022) and evaluate He loss due to earthquake processes (Armstrong et al., 2022).

The low but broad temperature sensitivity, or closure temperature (T<sub>C</sub>), of the ZHe system (~25–225 °C) is controlled in part by the accumulation and annealing of radiation damage, which is a function of zircon grain chemistry and the thermal history (Guenthner et al., 2013; Ginster et al., 2019). Radiation damage is a disruption to atomic structure of the crystal lattice due to actinide decay (Holland and Gottfried, 1955; Woodhead et al., 1991; Nasdala et al., 1995; Nasdala et al., 2001), and this damage anneals (recovers) with increased temperature (Zhang et al., 2000; Guenthner et al., 2013; Ginster et al., 2019). Damage

E-mail address: ema.armstrong@usu.edu (E.M. Armstrong).

a Department of Geosciences, Utah State University, USA

<sup>&</sup>lt;sup>b</sup> Department of Earth Science and Environmental Change, University of Illinois at Urbana-Champaign, USA

<sup>\*</sup> Corresponding author.

accumulation results in visual metamictization, or destruction of the ordered crystal lattice that is visible in plane polarized light (Holland and Gottfried, 1955; Woodhead et al., 1991; Garver and Kamp, 2002; Ewing et al., 2003). Provided zircon crystals experience the same thermal history, the measured effective U concentration (i.e., eU; eU = [U] + 0.238\*[Th]; Cooperdock et al., 2019) corresponds to the radiation damage preserved in a grain. Defining relationships between eU, radiation damage, and ZHe date is useful for reconstructing a sample's thermal history and requires analyzing zircon grains with a broad range of eU and radiation damage.

Prior work revealed intentionally selecting zircon grains for ZHe analysis from a sample with a spectrum of visual metamictization yielded a range in eU up to 2000 ppm that is required for developing a ZHe date-eU trend (Ault et al., 2018). In this past study, increasing visual metamictization generally corresponded with increasing eU in each of the Paleoproterozoic and Archean samples investigated, and some samples yielded negative ZHe date-eU relationships, common for rocks of this age, reflecting linked radiation damage and He diffusivity. However, other Paleoproterozoic samples yielded uniform dates regardless of eU and increasing visual metamictization with increasing eU. This suggests He loss may be decoupled from damage in these samples due to their thermal history and/or visual metamictization is not a reliable qualitative proxy for preserved radiation damage.

Here we advance the previous study by comparing zircon visual metamictization with radiation damage quantified by Raman spectroscopy analyses in a suite of zircon grains (n = 92). We use zircon crystals from six samples with Proterozoic and Archean crystallization ages from Ault et al. (2018), together with a detrital sample comprising grains with likely Phanerozoic crystallization ages from Armstrong et al. (2022). Prior ZHe analyses from these samples yielded three different types of ZHe date-eU relationships. We evaluate visual metamictization across samples and between studies (i.e., analysts), and report new Ramancalculated radiation damage data including 2-dimensional (2-D) maps from a subset of grains, cathodoluminescence images, and ZHe data (n= 21 individual analyses) to document damage-diffusivity-visual metamictization relationships. We show that, to first order, visual metamictization is a qualitative proxy for radiation damage lending veracity to this zircon grain selection approach. However, samples characterized by limited intrasample variation in visual metamictization, and/or substantive intragrain eU zonation and thus spatially heterogeneous damage, may not yield clear relationships between visual metamictization and damage calculated from Raman spectroscopy.

#### 2. Background

### 2.1. Radiation damage and visual metamictization in zircon

Radiation damage in zircon crystals distorts or bends bonds in the crystal structure and occurs due to recoil of a large nuclei (i.e., <sup>238</sup>U, <sup>235</sup>U, <sup>232</sup>Th, and other isotopes in these decay chains) from alpha decay, ejection of an alpha particle from a heavy nucleus, or spontaneous fission and resulting tracks (Hurley, 1952; Ewing et al., 2003; Reiners, 2005; Guenthner et al., 2013; Ketcham et al., 2013). Alpha recoil damage is volumetrically the most significant form of damage, and thus is considered a proxy for total radiation damage (Shuster and Farley, 2009). Damage anneals (i.e., recovery of the crystal lattice) as a function of temperature (Nasdala et al., 1995; Zhang et al., 2000), thus effective radiation damage is a function of a grain's U and Th content and the thermal history it experienced (Guenthner et al., 2013; Ketcham et al., 2013). We use the term accumulated radiation damage to represent all the damage a grain has experienced in its "lifetime" (no annealing), and we use the term effective radiation damage to represent observed damage, reflecting both accumulation and annealing. Most zircons are geochemically zoned (e.g., Corfu et al., 2003), including zoned with respect to eU (Hanchar and Miller, 1993; Hourigan et al., 2005; Orme et al., 2015) thus effective radiation damage (Guenthner et al., 2013; Danišík et al., 2017; Anderson et al., 2020). The magnitude of intragrain variability in effective damage depends on the eU content of different zones and the thermal history.

The appearance of zircon grains also changes with increasing disruption to the crystal lattice. Visual metamictization is readily observed with a stereoscope in plane-polarized light as a darker appearance (or color) and loss of transparency (Gastil et al., 1967; Garver and Kamp, 2002; Ewing et al., 2003; Marsellos and Garver, 2010; Ault et al., 2018). Variations in zircon color can also reflect different trace element contents (Kempe et al., 2016). A prior study evaluated relationships between zircon color attributed to radiation damage, color "resetting," and track annealing in detrital zircon fission track grain populations, but did not quantify radiation damage (Garver and Kamp, 2002). More recent work demonstrated a general relationship between the degree of visual metamictization in a zircon crystal and eU in Proterozoic and Archean zircon (Ault et al., 2018). Across this dataset, grains with low visual metamictization are transparent and have low eU; moderate visual metamictization crystals appear translucent and commonly honey brown, and yield moderate eU values. Highly metamict grains are black-brown and opaque, and have relatively high eU values. Importantly, the connection between visual metamictization and eU is qualitative as the intrasample range (or magnitude of variation) in visual metamictization, and thus eU, varies from sample to sample (Ault et al., 2018). Regardless, Ault et al. (2018) showed that purposefully selecting the range of observed visual metamictization in a given sample will produce a spread in eU (up to ~2000 ppm in Ault et al., 2018) that is useful for interpreting ZHe date-eU patterns. This approach has been successfully applied in other studies (e.g., McDermott et al., 2019; Flowers et al., 2020; Machado et al., 2021; Moser et al., 2021; Havranek and Flowers, 2022; McMillan et al., 2022; Thurston et al., 2022; Ronemus et al., 2023).

# 2.2. Zircon (U-Th)/He thermochronometry and relationships to radiation damage

Zircon He thermochronometry exploits the temperature- and timedependent diffusion of radiogenic He through the crystal lattice. The T<sub>C</sub> of the ZHe system for a low to moderately damaged zircon (i.e., Fish Canyon Tuff zircon,  $\sim$ 28 Ma,  $\sim$ 500 ppm eU) is  $\sim$ 160–200 °C, assuming a 10 °C/Ma cooling rate (Reiners et al., 2004). Aside from temperature and time, radiation damage is the main control on He diffusion, and thus a grain's T<sub>C</sub> (Guenthner et al., 2013; Ketcham et al., 2013). Diffusion and annealing experiments on grains with a range of radiation damage demonstrate a wider range of  $T_C$  of ~25–225 °C, assuming a 10 °C/Ma cooling rate (Guenthner et al., 2013; Ginster et al., 2019). This range reflects the evolution of He diffusivity with increased damage accumulation. Initially, accumulated damage disrupts c-axis-parallel diffusion pathways resulting in increased He retentivity and thus T<sub>C</sub>. Then, damage accumulation reaches a threshold (i.e., percolation threshold) where damaged portions of the crystal lattice become interconnected, diffusivity increases, and T<sub>C</sub> decreases (Guenthner et al., 2013; Ketcham et al., 2013).

Provided zircon grains experienced the same thermal history, the measured eU concentration provides a qualitative approximation of the effective radiation damage. The relationships between effective radiation damage, eU, He retentivity, and ZHe date in a given sample, and resulting ZHe date-eU patterns, have been described in many prior studies (e.g., Guenthner et al., 2013; Orme et al., 2016; Guenthner et al., 2017; Johnson et al., 2017; Ault et al., 2018). Briefly here, positive and/or negative relationships between eU and ZHe date are nonlinear and develop in samples that experienced a common, protracted thermal history such as slow cooling, residence within the ZHe partial retention zone, and/or reheating (e.g., Guenthner et al., 2013; Orme et al., 2016; Powell et al., 2016; Johnson et al., 2017; Ault et al., 2018; DeLucia et al., 2018; Flowers et al., 2020; Peak et al., 2021; Havranek and Flowers, 2022; Thurston et al., 2022). Negative ZHe date-eU trends are

commonly observed in ancient (i.e., Proterozoic, Archean) crystalline basement. Positive ZHe date-eU patterns are not commonly reported but have been documented in Phanerozoic samples that experienced modest reheating (e.g., Armstrong et al., 2022). Uniform ZHe dates regardless of eU concentration (hereafter referred to as a "flat" date-eU trend for brevity) reflect complete He loss during a phase of rapid cooling (e.g., Guenthner et al., 2014; Ault et al., 2018; Moser et al., 2021). Heterogeneous intracrystalline eU and thus effective radiation damage, as well as fluid inclusions and lattice vacancies, influence He diffusion in zircon and can complicate ZHe date-eU patterns (e.g., Danišík et al., 2017; Anderson et al., 2020).

Prior work highlighted two overarching relationships between visual metamictization, eU, assumed effective radiation damage, and He diffusion (i.e., ZHe date) in a suite of samples with Proterozoic and Archean crystallization ages (Ault et al., 2018; Moser et al., 2021). In all samples, increasing visual metamictization corresponded with increasing eU. Some samples yielded negative ZHe date-eU patterns interpreted to reflect coupled effective damage and He diffusivity. But other samples exhibited a flat ZHe date-eU trend, suggesting either He diffusion may be decoupled from effective damage or the degree of visual metamictization does not always capture effective radiation damage. These observations motivate our work to document the relationships between visual metamictization to not just eU (i.e., Ault et al., 2018) but also effective radiation damage.

#### 2.3. Estimating radiation damage in zircon

Alpha dose, or the measure of alpha recoil damage, can be estimated in a zircon grain using the U-Pb crystallization age, from models of radiation damage accumulation and annealing, or with Raman spectroscopy. Using a zircon crystal's U-Pb crystallization age and eU concentration (Holland and Gottfried, 1955) provides an estimate of the total possible accumulated damage (i.e., an upper bound), as some damage is likely annealed over a grain's "lifespan." Alternatively, the zircon radiation damage accumulation and annealing model (Guenthner et al., 2013) implemented in HeFTy (Ketcham, 2005) and Matlab (Guenthner, 2021) calculates alpha dose for a given eU concentration and thermal history. This approach accounts for annealing and uses the temperature at which zircon fission tracks anneal (Yamada et al., 2007) as a proxy for the temperature at which alpha recoil damage anneals (Guenthner et al., 2013). A more recent damage annealing model with kinetics that vary as a function of damage level (Ginster et al., 2019) also calculates alpha dose through a prescribed thermal history in Matlab (Guenthner, 2021).

Raman spectroscopy is useful for quantifying effective radiation damage because it measures the present-day, in-situ crystallinity of zircon grains resulting from the full thermal history that the grain experienced (Nasdala et al., 1995). Specific zircon Raman spectra peaks are sensitive to changes in crystallinity. The 1008 cm<sup>-1</sup> Raman peak will broaden and shift to lower wave number as the degree of crystallinity decreases (Nasdala et al., 2001). Other Raman peaks, such as at 439 cm<sup>-1</sup> and 357 cm<sup>-1</sup>, also show a correlation with effective damage (Anderson et al., 2020). Here we focus only on the 1008 cm<sup>-1</sup> band and use the full width at half maximum (FWHM) value of the 1008 cm<sup>-1</sup> peak to calculate alpha dose using Eq. (2) from Váczi and Nasdala (2017), as described in Section 3.3.

#### 3. Samples and analytical methods

#### 3.1. Samples

We used mineral separates from a suite of seven samples with previously reported ranges in visual metamictization, eU, and ZHe dates: six samples are from Ault et al. (2018) and one from Armstrong et al. (2022) (Figs. S1, S2; Table S1). Four samples from Ault et al. (2018) have negative ZHe date-eU trends: Cumberland Batholith of southwestern

Baffin Island, Canada (A10-42; ~1.9 Ga; Jackson et al., 1990; Rayner et al., 2012); Rae craton granitic gneiss from north-central Baffin Island (A10-3, ~3.0 Ga; Bethune and Scammel, 2003); Sandia granite from the Sandia Mountains, New Mexico (MC14s6; ~1.4 Ga; Kirby et al., 1995); and Boulder Creek granodiorite from the Front Range, Colorado (A12-8; ~1.7 Ga; Premo and Fanning, 2000). Two samples from Ault et al. (2018) are characterized by a flat ZHe date-eU trend. Both are North American crystalline basement gneiss exposed in Mecca Hills, California (PCFs6, MHS1; ~1.8 Ga; Moser et al., 2021; Table S1; Fig. S1). Sample EA20-3A from Armstrong et al. (2022) has a positive ZHe date-eU pattern and is from the Punchbowl Formation, a conglomeratic sandstone exposed in the San Gabriel Mountains, California with likely zircon U-Pb crystallization ages of ~150 Ma (Ingersoll et al., 2013; Coffey et al., 2019). Samples were previously crushed and separated using standard mineral separation techniques; see Supplemental Material for more details.

#### 3.2. Grain selection and classification using visual metamictization

The analyst (Armstrong) that selected the grains for this study is different from the analyst that selected grains in Ault et al. (2018) but the same for Armstrong et al. (2022). For each sample, 10 to 14 grains that encompass the range of visual metamictization within that sample were selected using the approach of Ault et al. (2018), plane-polarized light, and a Leica stereoscope. Care was taken to not consider apparent opacity due to grain relief and to avoid grains with visible cracks. The analyst arranged crystals from lowest to highest visual metamictization and assigned an increasing "Z number" to each grain. Z numbers cannot be compared between samples, as they are relative within a given sample.

We also classify visual metamictization using the luminosity measurement function in Adobe Photoshop. Luminosity values are normalized to a value of 157 (maximum luminosity measured across all grains) to compare relative color change of grains within and between samples and we refer to this as "normalized luminosity." Detailed normalized luminosity methodology is present in the Supplemental Material. In theory, this approach should allow for the reduction of user bias and comparison of different analysts. However, grain relief and flaws (i.e., cracks, chips, staining), as well as different white balance routines in various stereoscopic camera software introduce additional luminosity variations. Thus, although we briefly describe relationships between luminosity and calculated damage in Section 5.1, we prefer and use Z number to indicate the spectrum and increase in intrasample visual metamictization.

### 3.3. Raman spectroscopy methods and damage calculations

Raman spectra were collected using a HORIBA Raman spectrometer in the Mineral Microscopy and Spectroscopy Laboratory (M<sup>2</sup>SL) at Utah State University. We collected three individual Raman spectra along the c-axis of the external portion of all zircon grains and three individual spectra along the c-axis of the internal portion (cross-section) of 77% of the grains. The remaining 33% of grains were analyzed for (U-Th)/He thermochronometry. We did not collect spectra from the internal portion of the grains that were analyzed for (U-Th)/He thermochronometry because routine, bulk (U-Th)/He analysis consumes the entire grain. Because we aim to directly compare our ZHe dates with those of Ault et al. (2018) and Armstrong et al. (2022) that were acquired by bulk analyses, we prefer to also analyze whole grains. Internal Raman measurements require polishing away a portion of the grain, which introduces additional uncertainty to the FT correction on bulk (U-Th)/He analyses. Thus, we do not have internal Raman measurements for the small subset of grains that we dated.

We intentionally chose to collect multiple point spectra (n = 480) instead of detailed, 2-D Raman maps for each grain for several reasons. Our objective with this multi-spot approach is to provide a *first-order* 

evaluation of how spatial variations in Raman spectra (i.e., variations in effective damage due to U and Th zonation) might impact the relationships between visual metamictization and effective radiation damage. Although we recognize most zircon crystals are zoned, the aim of this study is not to provide a detailed characterization of spatial variability in damage in each grain. In addition, using our analytical protocols (described briefly below and in detail in the Supplemental Material), multiple spot analyses per grain are markedly more time efficient than 2-D maps. However, we also acquired 2-D Raman maps on the internal portions of three grains (MC14s6 Z14, PCFs6 Z13, and EA20–3A Z11) to compare with our six point analyses from each of these same zircon crystals to further evaluate the robustness of our multi-spot analytical approach.

To prepare the samples for surface (external) Raman analysis, grains were placed on double-sided Scotch office tape on a glass slide with sample names and Z numbers noted. Spectra on the external portion of each grain were acquired at three points parallel to the c-axis including near each tip and in the grain center. For internal analyses, grains were removed from the sticky tape, mounted in epoxy in  $1^{\prime\prime}$  ring forms with their c-axes parallel to the mount surface and polished to their approximate midsection using diamond grit paper down to  $1~\mu m$ . After polishing, we targeted three evenly-spaced spots from center to the edge of the grain. For all analyses, grains were oriented with their c-axis perpendicular to the incident beam (Anderson et al., 2020) and for individual analyses, care was taken to avoid any visible flaws such as cracks or inclusions.

We used a Scientific LabRAM HR Evolution confocal dispersive Raman spectrometer in the M<sup>2</sup>SL, which was calibrated daily using a silicon wafer standard and its 520.7 cm<sup>-1</sup> Raman peak. All individual spectra were acquired using a 633 nm laser, 1800 gr/mm diffraction grating,  $50 \times long$  working distance or  $50 \times (for A10-42 only)$  objectives, hole size of 100  $\mu m$ , 2 accumulations, an accumulation time between 3 and 15 s, and a 100–1800 cm<sup>-1</sup> spectral range. 2-D Raman maps were collected using the same parameters as for point analyses, but with exclusively the 50× objective, 5 or 7 s accumulation time per measurement, and a grid spacing of 5  $\mu m$ . Complete acquisition parameters for each point analysis and map are provided in Table S2, and detailed information about the M2SL Raman spectrometer is provided in the Supplemental Material. Spectra were corrected using appropriate baseline corrections in LabSpec6 software. The LabSpec6 Gaussian-Lorentzian peak fitting function was used to estimate the Raman shift and the FWHM of relevant peaks.

Effective radiation damage (alpha dose) was estimated from the equation with the general form:

$$\nu_3(SiO_4)FWHM = A_1 - A_2exp^{-B_{FWHM}D} \tag{1}$$

where  $A_1$ ,  $A_2$ , and  $B_{FWHM}$  are scaling factors,  $\nu_3(SiO_4)FWHM$  is the FWHM of the  $\nu_3$ , or 1008 cm<sup>-1</sup> peak, and D is the alpha dose. Váczi and Nasdala (2017) determined these scaling factors and use the equation:

$$\nu_3(SiO_4)FWHM = 34.96 - 33.16exp^{-(5.32 \times 10^{-19})D}$$
 (2)

Rearranged to:

$$D = \ln((34.96 - \nu_3(SiO_4)FWHM)/33.16))/(-5.32 \times 10^{-19})$$
(3)

where FWHM values for the  $1008~\rm cm^{-1}$  Raman band that are  $> 34.96~\rm cm^{-1}$  or those with uninterpretable spectra are considered completely amorphous (Váczi and Nasdala, 2017), and assigned FWHM values of  $34.96~\rm cm^{-1}$  for the purpose of alpha dose calculations. To calculate average alpha dose for each grain (for both point analyses and maps) we first determined the alpha dose for each spot, then averaged these values.

#### 3.4. Cathodoluminescence imaging

Cathodoluminescence (CL) imaging of zircon grains mounted in epoxy and polished to their midsection was used to identify variations in effective radiation damage in zircon crystals. Heavier elements (e.g., U, Th, and other rare Earth elements) activate CL; however, crystal defects decrease CL activation (i.e., regions with more radiation damage appear darker in CL; Ewing et al., 2003; Nasdala et al., 2003). Although these factors may counteract one another, CL imaging still reveals intragrain zonation patterns that may influence relationships between visual metamictization and Raman-measured damage. Zircon epoxy mounts were carbon coated then imaged using an FEI NovaNano 600 scanning electron microscope equipped with a Gatan Mini CL detector in the Department of Physics at the University of Utah.

#### 3.5. Zircon (U-Th)/He thermochronometry

Three zircon grains from each sample that capture low, moderate, or high visual metamictization for the sample were selected for (U-Th)/He analyses. After collecting three external Raman analyses for each of these grains, crystals were plucked from double-sided tape, imaged, and measured using a stereoscope and Leica software, and then placed into 1 mm Nb tubes in the M²SL at Utah State University. All grains were analyzed for their bulk U, Th, and He contents at the Arizona Radiogenic Helium Dating Laboratory (ARHDL) at the University of Arizona following standard degassing, spiking, and dissolution protocols (Guenthner et al., 2016). We applied parent-isotopic specific alpha ejection correction factors computed using grain measurements, and the equations and alpha stopping distances reported in Hourigan et al. (2005), assuming a homogeneous distribution of U and Th. Analytical details are provided in Supplemental Material and our study-specific workflow for all methods provided in Fig. S3.

#### 4. Results

#### 4.1. Visual metamictization patterns

For each sample, the selected zircon crystals reflect different spectrums of visual metamictization across Z numbers (Fig. 1) and the observed visual metamictization variability for the entire mineral separate. In plane polarized light, crystals generally range in appearance from clear to brown-black, transparent to opaque, and have faceted to rounded terminations, respectively. Importantly, the intrasample range in visual metamictization differs for each sample, with different, relative "minimum" and "maximum" visual metamictization. Some samples are dominated by grains with similar visual metamictization levels (Fig. 1). Selected grains for each sample capture a comparable range in visual metamictization as reported in prior studies, even though grains were selected by either two different analysts or in different sessions (Fig. S2; Ault et al., 2018; Armstrong et al., 2022). Z number increases with decreasing normalized luminosity (Fig. S5).

In detail, zircon grains in sample A10–42 range from low to high visual metamictization, with most of the successive Z-numbered zircon having a slightly different appearance (Fig. 1). Sample A10–3 is dominated by grains with similar medium to high visual metamictization (Z2 to Z6), and grains with similar very high visual metamictization (Z7 to Z14). MC14s6 is characterized by a progressive increase in visual metamictization with increasing Z number. The visual metamictization in sample A12–8 is similar to A10–3, with only Z1 characterized by low metamictization. Multiple grains in A12–8 (Z6 to Z10) have similar medium-high visual metamictization levels, but Z11 and Z12 have very high metamictization. Samples PCFs6 and MHS1 each yield a modest spectrum of visual metamictization, but a greater proportion of the grains are less visually metamict than other samples. In addition, Z1 to Z8 in sample MHS1 exhibit a similar level of low visual metamictization. Sample EA20–3A also has a high proportion of low visual

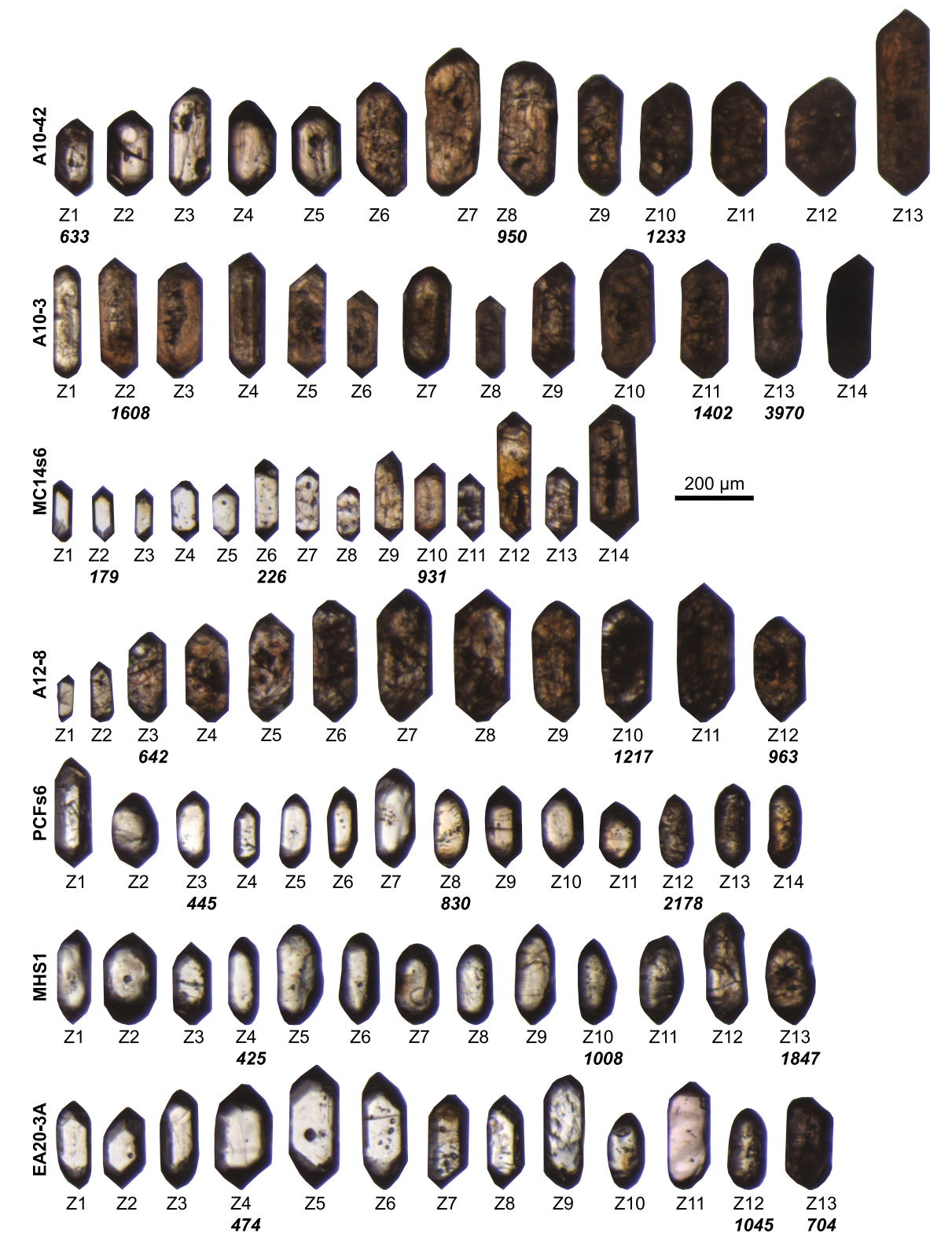
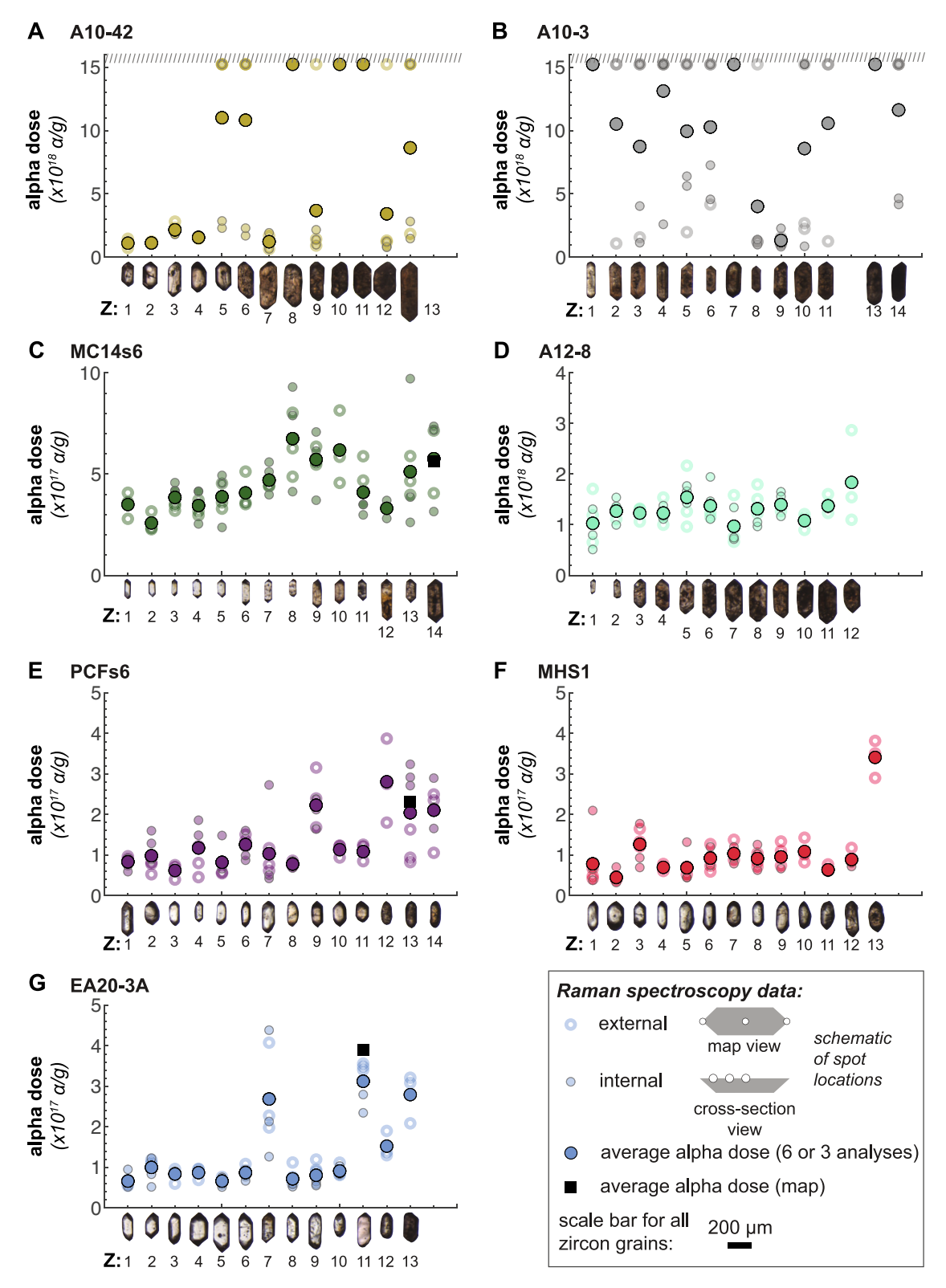


Fig. 1. Plane polarized light stereoscopic photos of selected zircon grains that span the spectrum of visual metamictization observed within each sample. Z number (relative visual metamictization) reported below each grain, with eU (ppm, bold italics) for a subset of grains.

metamictization grains with only Z7, Z11, Z12, and Z13 classified as medium to high visual metamictization.

4.2. Effective radiation damage calculated from Raman spectroscopy and relationships to visual metamictization

Figure 2 and Table S3 report all calculated alpha dose values from our multi-spot internal and external Raman spectroscopy transects for each grain, and we provide the minimum and maximum values from



**Fig. 2.** All internal (transparent filled symbols) and external (transparent open symbols) alpha dose values calculated from Raman spectroscopy as a function of grain Z number with stereoscopic plane polarized light images of the associated grains for each sample. Average alpha dose of six or three analyses (filled opaque circle) and average alpha dose from the ensemble of individual measurements in maps of select grains shown for comparison. Different y-axis scales used to highlight trends and scatter about those trends. Cross hatch pattern in A and B indicates maximum possible alpha dose.

internal and external analyses for each grain in Table 1. Because the maximum possible calculated alpha dose is  $\sim 1.52 \times 10^{19}$   $\alpha/g$  (e.g., Váczi and Nasdala, 2017), uninterpretable spectra reflecting alpha doses that exceed this threshold were assigned the maximum alpha dose, such

as grains in samples A10–42 and A10–3. Samples A10–42, A10–3, PCFs6, MHS1, and EA20–3A have more than an order of magnitude intrasample spread in calculated alpha dose, and samples A12–8 and MC14s6 have nearly an order of magnitude intrasample range in alpha

 Table 1

 Average alpha dose and zircon (U-Th)/He thermochronometry data from seven samples.

	External		Internal												
Sample and z number <sup>a</sup>	Minimum alpha dose α/g	Maximum alpha dose α/g	Minimum alpha dose α/g	Maximum alpha dose α/g	eU <sup>b</sup>	Corrected (U-Th)/He date	(U-Th)/He date error <sup>c</sup>								
								egative ZHe date-e 10–42	U trend						
								1*	7.27E+17	1.45E+18	_	_	633	781	30
2	1.12E+18	1.24E+18	9.51E+17	1.17E+18	_	_	_								
3	2.14E+18	2.81E+18	1.80E+18	2.04E+18	_	_	_								
4	1.46E+18	1.62E + 18	1.39E+18	1.75E+18	_	_	_								
5	1.52E+19	1.52E+19	2.30E+18	1.52E+19	_	_	_								
6	1.52E+19	1.52E+19	1.69E+18	1.52E+19	_	_	_								
7	6.47E+17	1.69E+18	6.55E+17	1.92E+18	_	_	_								
8*	1.52E+19	1.52E+19	_	_	950	230	7								
9	9.18E+17	1.52E+19	9.87E+17	2.16E+18	_	_	_								
10*	1.52E+19	1.5238E+19	_	_	1233	173	5								
11	1.52E+19	1.5238E+19	_	_	_	_	_								
12	1.20E + 18	1.52E+19	7.77E+17	1.22E+18	_	_	_								
13	1.84E + 18	1.52E+19	1.47E+18	1.52E+19	_	_	_								
10–3															
1	1.52E+19	1.52E+19	1.52E+19	1.52E+19	_	_	_								
2*	1.08E+18	1.52E+19	=	_	1608	41.4	1.2								
3	1.56E+18	1.52E+19	1.14E+18	1.52E+19	_	=	_								
4	1.52E+19	1.52E+19	2.60E+18	1.52E+19	_	_	_								
5	1.97E+18	1.52E+19	5.62E+18	1.52E+19	_	_	_								
6	4.16E+18	1.52E+19	4.57E+18	1.52E+19	_	_	_								
7	1.52E+19	1.52E+19	1.52E+19	1.52E+19	_	_	_								
8	1.21E+18	1.52E+19	9.90E+17	4.00E+18	_	_	_								
9	1.03E+18	1.56E+18	8.29E+17	2.28E+18	_	_	_								
10	2.24E+18	1.52E+19	8.59E+17	1.52E+19	_	_	_								
11*	1.26E+18	1.52E+19	_	_	1402	68.5	2.0								
13*	1.52E+19	1.52E+19	_	_	3970	7.91	0.23								
14	1.52E+19	1.52E+19	4.17E+18	1.52E+19	_	_	_								
IC14s6	:			= 1 = -											
1	2.79E+17	4.08E+17	-	_	_	_	_								
2*	2.28E+17	3.16E+17	_	_	179	146	5								
3	3.20E+17	3.52E+17	4.17E+17	4.58E+17	_	_	_								
4	2.96E+17	3.72E+17	2.54E+17	4.15E+17	_	_	_								
5	3.29E+17	4.54E+17	2.37E+17	4.94E+17	_	_	_								
6*	3.51E+17	5.13E+17	_	_	226	287	8								
7	4.39E+17	4.70E+17	3.98E+17	5.59E+17	_	_	_								
8	4.87E+17	8.03E+17	4.14E+17	9.30E+17	_	_	_								
9	5.47E+17	6.36E+17	3.71E+17	7.08E+17	_	_	_								
10*	4.57E+17	8.15E+17	-	-	931	32.4	0.8								
11	4.07E+17	5.88E+17	2.99E+17	3.50E+17	_	_	-								
12	-	-	2.81E+17	3.70E+17	_	_	_								
13	3.98E+17	5.89E+17	2.62E+17	9.71E+17	_	_	_								
14	4.06E+17	7.15E+17	3.15E+17	7.36E+17	_	_	_								
12–8															
1	6.54E+17	1.71E+18	5.11E+17	1.31E+18	_	_	_								
2	1.11E+18	1.31E+18	9.96E+17	1.54E+18	_	_	_								
3*	1.06E+18	1.32E+18	9.90E+17 -	- -	- 642	- 75.2	2.0								
4	1.00E+18 1.00E+18	1.54E+18	- 1.11E+18	- 1.38E+18	-	-	_								
5	9.62E+17	2.17E+18	1.43E+18	1.77E+18	_	_	_								
6	9.02E+17 1.15E+18	1.33E+18	1.43E+18 1.11E+18	1.77E+18 1.94E+18	_	_	_								
7	6.64E+17	1.58E+18	7.16E+17	1.34E+18	_		_								
8	1.22E+18	1.80E+18	9.67E+17	1.35E+18	_	_	_								
9	1.27E+18	1.38E+18	1.17E+18	1.65E+18	_	_	_								
10*	8.98E+17	1.21E+18	1.1/E+16 -	1.03E+16 -	- 1217	- 78.3	- 2.1								
11	1.23E+18	1.60E+18	- 1.32E+18	- 1.34E+18	-	/o.3 _	<b>2.1</b> –								
12*	1.23E+18 1.10E+18	2.87E+18	1.32E+18 -	1.34E+18 -	- 963	39.6	1.0								
10	1.10ET10	2.0/ £⊤10	_	_	903	55.0	1.0								
at 711a deservit	A														
lat ZHe date-eU tre CEs6	na														
CFs6	0.000 + 16	0.605 + 16	E 00E : 16	0.10E+16											
1	8.82E+16	9.69E+16	5.89E+16	9.10E+16	_	_	_								
2	5.23E+16	8.13E+16	8.85E+16	1.60E+17	-	-	-								
3*	3.93E+16	7.49E+16	-	-	445	27.6	0.8								
4	4.52E+16	1.22E+17	1.22E+17	1.86E+17	-	-	_								
5	5.47E+16	8.09E+16	6.59E+16	1.48E+17	-	-	-								
6	1.22E+17	1.51E+17	8.70E+16	1.60E+17	-	-	-								
7	6.13E+16	1.17E+17	4.20E+16	2.73E+17	-	-	-								
8	7.28E+16	8.58E+16	6.77E+16	8.49E+16	-	-	-								
9	1.68E+17	3.16E+17	1.64E+17	2.38E+17	-	-	-								
10*	9.37E+16	1.23E+17	_	_	830	24.6	0.7								

(continued on next page)

Table 1 (continued)

Sample and z number <sup>a</sup>	External		Internal				
	Minimum alpha dose α/g	Maximum alpha dose α/g	Minimum alpha dose α/g	Maximum alpha dose	eU <sup>b</sup>	Corrected (U-Th)/He date	(U-Th)/He date error <sup>c</sup>
12*	1.80E+17	3.87E+17	_	_	2178	21.8	0.6
13	8.24E+16	1.63E+17	2.71E+17	3.24E+17	_	_	_
14	1.05E+17	2.49E+17	1.65E+17	2.90E+17	_	_	_
MHS1							
1	4.15E+16	6.61E+16	3.73E+16	2.10E+17	_	_	_
2	3.79E+16	4.64E+16	3.19E+16	7.03E+16	_	_	_
3	1.21E+17	1.65E+17	6.91E+16	1.77E + 17	_	_	_
4*	6.05E + 16	7.78E+16	_	_	425	23.7	0.8
5	5.20E+16	7.11E+16	4.43E+16	1.32E+17	_	_	_
6	5.91E+16	1.27E+17	7.44E+16	1.20E+17	_	_	_
7	8.79E+16	1.38E+17	7.85E+16	1.20E+17	-	_	_
8	7.10E+16	1.04E+17	6.26E+16	1.26E+17	_	_	_
9	7.36E+16	1.33E+17	6.63E+16	9.50E+16	_	_	_
10*	8.19E+16	1.43E+17	_	_	1008	26.0	0.7
11	6.13E+16	7.68E+16	5.73E + 16	6.14E+16	-	_	_
12	8.85E+16	1.18E+17	7.16E+16	8.54E+16	-	_	_
13*	2.90E+17	3.82E + 17	-	-	1847	24.0	0.7
Positive ZHe date-el	U trend						
EA20-3A							
1	5.44E+16	6.89E+16	5.19E+16	9.49E+16	-	-	-
2	1.11E+17	1.19E+17	5.18E+16	1.23E+17	-	-	-
3	5.97E+16	9.61E+16	8.44E+16	9.03E+16	-	_	_
4*	6.89E+16	9.63E+16	_	_	474	64.9	1.8
5	6.80E+16	7.64E+16	5.15E+16	7.54E+16	-	_	_
6	8.35E+16	1.08E+17	6.66E+16	9.38E+16	-	_	_
7	1.98E+17	4.08E+17	1.26E+17	4.39E+17	_	_	_
8	6.05E + 16	1.12E+17	5.23E+16	6.98E+16	-	_	_
9	9.11E+16	1.19E+17	5.51E+16	6.49E+16	-	_	_
10	8.10E+16	1.12E+17	8.35E+16	1.03E+17	-	_	_
11	3.41E+17	3.56E+17	2.35E+17	3.15E+17	-	_	_
12*	1.30E+17	1.90E+17	_	_	1045	72.6	1.8
13*	2.09E+17	3.21E+17	_	_	704	57.9	1.6

a \*Indicates grains analyzed for (U-Th)/He, thus have external alpha dose only because the grains were consumed during analyses.

dose (Table 1). Calculated alpha dose values are overall highest in A10–42 and A10–3, followed by A12–8 and MC14s6 with measurements that exceed those in samples PCFs6, MHS1, and EA20–3A. Sample MHS1 has the lowest calculated alpha dose across all measurements (Table 1). For most samples, there is a weak trend between normalized luminosity and alpha dose (Fig. S6; Table S3).

Raman-calculated alpha dose generally increases with increasing Z number for most samples (Fig. 2), and, similarly, FWHM increases with Z number (Fig. S4). The positive relationship between Z number and associated alpha dose is best expressed in samples MC14s6, PCFs6, and EA20–3A. Samples A12–8 and MHS1 yield weak positive trends and many grains yield overlapping alpha dose values across adjacent Z numbers in each of these samples. The overall trend between Z number and alpha dose is poorly defined in A10–42 and there is no relationship between alpha dose and Z number in A10–3.

In order to provide a first order assessment of effective radiation damage zonation in each grain, we visualize internal alpha dose as a function of external alpha dose, where the 1:1 line in Figs. 3 and 4 represents a homogeneous alpha dose or damage distribution. In Fig. 3, average internal and average external values are shown and classified by Z number (note x- and y-axis scales are different for each sample to accentuate patterns). Fig. 4 shows all individual alpha dose values as well as associated averages classified by sample. These figures illustrate that there is variable spread along the 1:1 line from sample to sample. Some samples are characterized by grains with intracrystalline alpha dose values that plot near the 1:1 line and others show more scatter perpendicular to the line. For example, most grains in samples MC14s6,

A12–8, PCFs6, MHS1, and EA20–3A plot close to the 1:1 line. In contrast, most grains in A10–42 and A10–3 deviate from this line. Fig. 4 highlights that (1) samples characterized by higher overall damage have a higher intrasample spread in damage (e.g., compare tightly clustered red circles of MHS1 with the position of green circles of A12–8 or the gray circles of A10–3), and (2) when considering the full dataset, intragrain variability in damage also increases with increasing damage value. For example, A10–42 and A10–3 have the largest intragrain variability of internal and external damage, consistent with observations from Fig. 2. For samples A10–42 and EA20–3A, calculated external alpha dose values are almost always higher than internal values (Fig. 3A, G).

## ${\it 4.3. \ Cathodolumine scence \ patterns}$

Cathodoluminesence patterns, which include oscillatory zonation and core-rim patterns, are variable between individual zircon grains within a sample and notably between samples (Fig. S7). Grains from samples A10–42 and A10–3 appear the darkest in CL. Detailed patterns are muted in CL in these samples, making it challenging to fully characterize the zoning in fine detail, but some grains exhibit faint oscillatory zoning. The majority of grains from samples A12–8 and MC14s6 have oscillatory zoning characterized by narrow bands; some grains in MC14s6 have distinct core-rim textures. Most grains in samples MHS1 and PCFs6 have large cores and a single, thick, distinct rim. In sample MHS1, grains Z1 and Z2 are bright in CL likely due to lower effective damage (e.g., Moser et al., 2021). Grains from sample EA20–3A have

<sup>&</sup>lt;sup>b</sup> eU is effective U, see Table S4 for details.

<sup>&</sup>lt;sup>c</sup> 2s analytical uncertainty propagated from U, Th, He measurements.

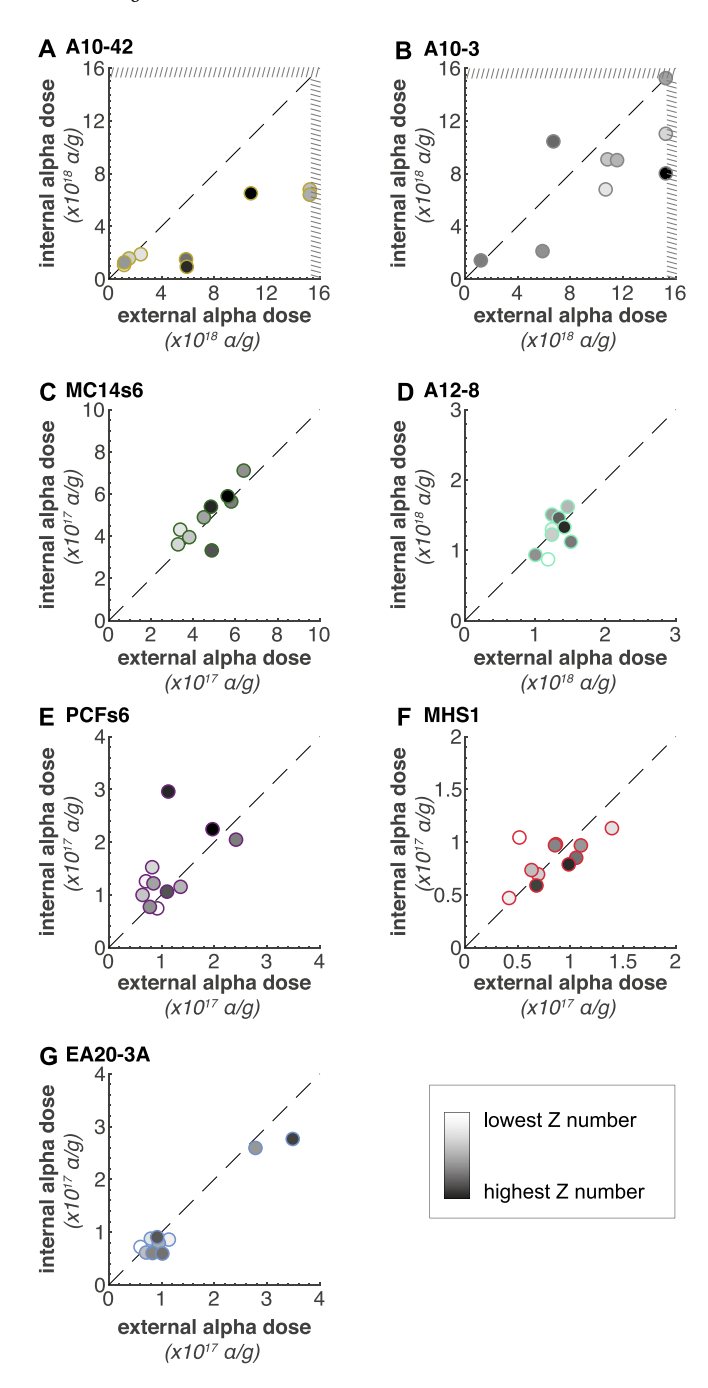


**Fig. 3.** Average internal alpha dose as a function of average external alpha dose, gray indicates increasing Z number values. Note change in x- and y-axis scales from sample to sample to accentuate patterns. Cross hatch pattern in A and B indicates maximum possible alpha dose.

variable CL patterns, which is expected because these detrital grains are likely of different provenance. Textures in this sample include oscillatory zoning, core-rim zoning, and irregular core textures. We note that zonation is observed in some grains with plane polarized light via stereoscope and these patterns are confirmed with CL maps (e.g., grain Z3 from sample A10–3; Figs. 1; S7).

### 4.4. 2-D Raman maps

We report 2-D maps of the measured FWHM values of the 1008 cm<sup>-1</sup> band from one grain in samples MC14s6 (Z14), PCFs6 (Z13), and EA20–3A (Z11) (Fig. 5, Tables S4, S5, S6). These grains were targeted

because they (1) are part of samples that yield well-defined negative, flat, and positive ZHe date-eU trends, respectively, as discussed in Section 4.5, (2) they exhibit distinct zoning patterns in CL (Figs. 5A, D, G, S7), and (3) they exhibit a range in calculated alpha dose from Raman analysis transects (Figs. 2, 3, 4).

MC14s6 Z14 has a generally high FWHM rim and low FWHM core, with narrow oscillatory zonation (Fig. 5B). PCFs6 Z13 exhibits a core with heterogeneous FWHM values surrounded by a thick ( $\sim\!15~\mu m$ ) rim of low FWHM values (Fig. 5E). EA20–3A Z11 is characterized by oscillatory FWHM values mirroring the CL map pattern, alternating from generally lower FWHM values in the core to higher FWHM values in the rim (Fig. 5H). We also report a histogram of all map measurements converted to alpha dose values.

We compare the 2-D map data with point analysis data from multispot transects in two ways. First, the ensemble of alpha dose measurements that comprise the 2-D maps for each of these grains overlaps and exceeds the range of measurements from the transects for each grain (Fig. 5C, F, I). Second, although we know these grains are zoned, we compare the average alpha dose values for both methods. The average alpha dose for MC14s6 Z14 is  $5.63\times10^{17}~\alpha/g$ , PCFs6 Z13 is  $2.31\times10^{17}~\alpha/g$ , and EA20–3A Z11 is  $3.90\times10^{17}~\alpha/g$  (Fig. 5C, F, I). Average values from maps are similar to the average of all of the point analyses for that grain: MC14s6 Z14 is  $5.76\times10^{17}~\alpha/g$ , PCFs6 Z13 is  $2.04\times10^{17}~\alpha/g$ , and EA20–3A Z11 is  $3.13\times10^{17}~\alpha/g$  (also shown in Fig. 5C, F, and I for reference; Fig. 2).

#### 4.5. Zircon (U-Th)/He thermochronometry and date-eU patterns

We report (U-Th)/He data from three zircon grains from each sample that represent relative low, moderate, and high visual metamictization for the sample (n=21 individual analyses; Tables 1, S7). The visual metamictization grain selection approach yields an intrasample range in eU concentration varying from 600 ppm to 2500 ppm internal spread across all samples (Figs. 6, 7, Table 1). These data fall within and outside the previously reported eU ranges for that sample (Figs. 6, 7; Table S3; Ault et al., 2018; Armstrong et al., 2022). Importantly, across the dataset, eU concentration generally increases with Z number (Fig. 6). There is a mismatch between increasing Z number and eU values in three samples (EA20–3A, A10–3, A12–8), but for samples EA20–3A and A12–8 the Z number is off by only one or two places. None of the samples show a clear trend between ZHe date and equivalent spherical radius, a proxy for grain size (Fig. S8).

Most samples yield a > 15% standard deviation of the mean ZHe date and we thus report the range of individual dates with their 2 s analytical uncertainty (Table 1). Our new ZHe data define and fall along previously reported ZHe date-eU trends for each sample (Fig. 7; Ault et al., 2018; Armstrong et al., 2022). These patterns include negative (A10–42, A10–3, MC14s6, A12–8), flat (PCFs6, MHS1), and positive (EA20–3A) ZHe date-eU patterns. Our new dates from EA20–3A define the 'plateau' portion of the positive ZHe date-eU trend. Only one analysis deviates from the patterns defined by new and published data (i.e., Z10 in A12–8).

#### 5. Discussion

# 5.1. Utility of visual metamictization grain selection approach to build ZHe date-eU patterns

The spectrum of visual metamictization and eU captured in the zircon grains in each sample in this study mirrors the range in visual metamictization and eU observed in the same samples in past studies (Figs. 6, S2; Ault et al., 2018; Armstrong et al., 2022). In most samples re-evaluated here, eU concentration increases with increasing Z number and thus intrasample visual metamictization (Fig. 6). This is because, for zircon grains that experienced the same thermal history, different parent isotope concentrations should accumulate variable radiation damage

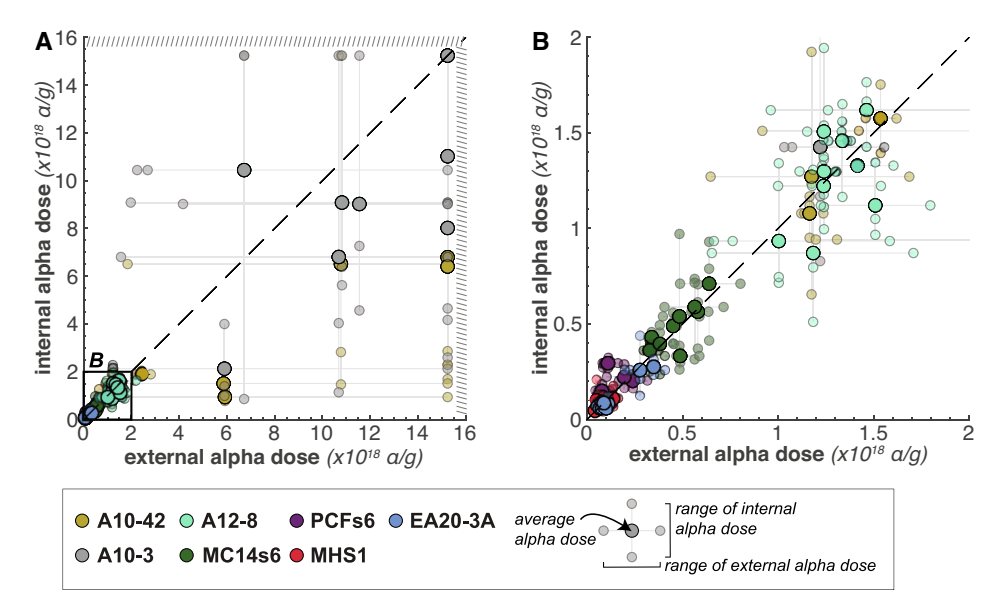


Fig. 4. Average (large symbols) and individual (transparent small symbols) internal alpha dose values as a function of external alpha dose for all samples. Black box on A denotes area of B. Cross hatch pattern in A indicates maximum possible alpha dose.

that is expressed as visual metamictization (Guenthner et al., 2013; Ault et al., 2018). As was observed in prior work, ascending Z number does not exactly correspond to increasing eU in some samples (Figs. 6, S2). For example, in sample A10–3, Z2 has a higher eU concentration than Z11 (Fig. 7B). We note that the eU difference between these two grains is only 200 ppm, which is small compared to the range in eU across all grains in that sample.

The Z number approach for grain selection is better suited than normalized luminosity to build visual metamictization-eU relationships. When selecting and ordering grains to assign Z numbers, the user can assess and ignore the contribution of apparent opacity from grain relief as well as avoid grains with cracks. These grain characteristics impact normalized luminosity values. For example, using a crude calculation of grain area, three of the seven samples have increasing normalized luminosity with increasing grain area, suggesting relief influences Photoshop-derived luminosity in some samples (Fig. S9). Normalized luminosity does allow for direct comparison between samples, but qualitative comparison of Z number between samples is possible. Even though Z number and normalized luminosity generally track one another for all samples (Fig. S5), and there is a weak relationship between luminosity and alpha dose (Fig. S6), we observe that Z number shows a clearer relationship (i.e., slope) with alpha dose than normalized luminosity. We thus prefer, emphasize, and use the Z number approach to generate a range in visual metamictization and eU values, but suggest that both techniques can be used for full sample characterization.

By using the visual metamictization zircon selection approach for ZHe analysis, our resulting ZHe dates overlap with and help further define previously reported ZHe date-eU trends from the same samples (Fig. 7; Ault et al., 2018; Armstrong et al., 2022). Specifically, our new data align with negative (A10–42, MC14s6, A12–8, A10–3), flat (PCFs6, MHS1), and positive (EA20–3A) ZHe date-eU relationships. Only one ZHe analysis does not fall along the trend defined by prior and new analyses; grain Z10 from sample A12–8 deviates from an overall negative ZHe date-eU trend (Fig. 7D), which may reflect the effects of eU zoning on effective radiation damage and He diffusion (see Section 5.2).

Prior work leveraged these ZHe date-eU patterns in simple "forward" thermal history models to place first-order constraints on the time-temperature histories of these samples (Ault et al., 2018; Armstrong et al., 2022), and we do not repeat that exercise here. Rather, we emphasize that the similarity in intrasample visual metamictization, eU

range (up to 2500 ppm in this study), and ZHe date-eU patterns generated from two different analysts or two different grain selection sessions (Figs. 7, S2), combined with successful application of the visual metamictization approach to produce ZHe date-eU trends in other studies (e. g., McDermott et al., 2019; Flowers et al., 2020; Machado et al., 2021; Havranek and Flowers, 2022; Thurston et al., 2022), collectively support that the visual metamictization should be applied to generate a range in eU values and ZHe date-eU patterns useful for interpretating detailed thermal histories.

# 5.2. Relationships between visual metamictization, effective radiation damage, and zoning

We advance prior work and show that the application of the visual metamictization zircon selection approach also yields a range in calculated alpha dose (i.e., effective radiation damage). We observe clear positive relationships between Z number and alpha dose in some samples (MC14s6, PCFs6, and EA20-3A; Fig. 2). In other samples, the trend between Z number and effective damage is not as strong (A12-8 and MHS1) or unclear (A10-42 and A10-3) (Fig. 2). Although visual metamictization tracks with eU and can be leveraged to build ZHe date-eU trends, the strength of the relationship between Z number and calculated alpha dose varies from sample to sample in our study for several reasons. First, visual metamictization, eU, and bulk ZHe dates are whole grain qualities or analyses. In contrast, the Raman analyses that underpin alpha dose calculations - whether multi-spot analyses along Caxis transects or the ensemble of individual spots comprising a 2-D map - are spatially isolated and site specific, and therefore impacted by eU and damage zonation. Second, damage annealing is also not linear with temperature and time. Finally, grain selection by visual metamictization is both qualitative and subjective.

Grain characteristics that influence assigned Z number, reported alpha dose, or both parameters, result in modest or unclear relationships between these parameters. Assigning ascending Z numbers is difficult when zircon crystals in a sample have similar levels of visual metamictization. A limited gradient in visual metamictization can occur at any damage level. Related, grains with similar metamictization in the same sample may have similar calculated alpha dose. It was difficult to assign Z numbers in samples MHS1 and A12–8 for these reasons. Grains Z1-Z8 in sample MHS1 are characterized by low visual metamictization and have overlapping calculated alpha dose values (Figs. 1, 2F). Crystals

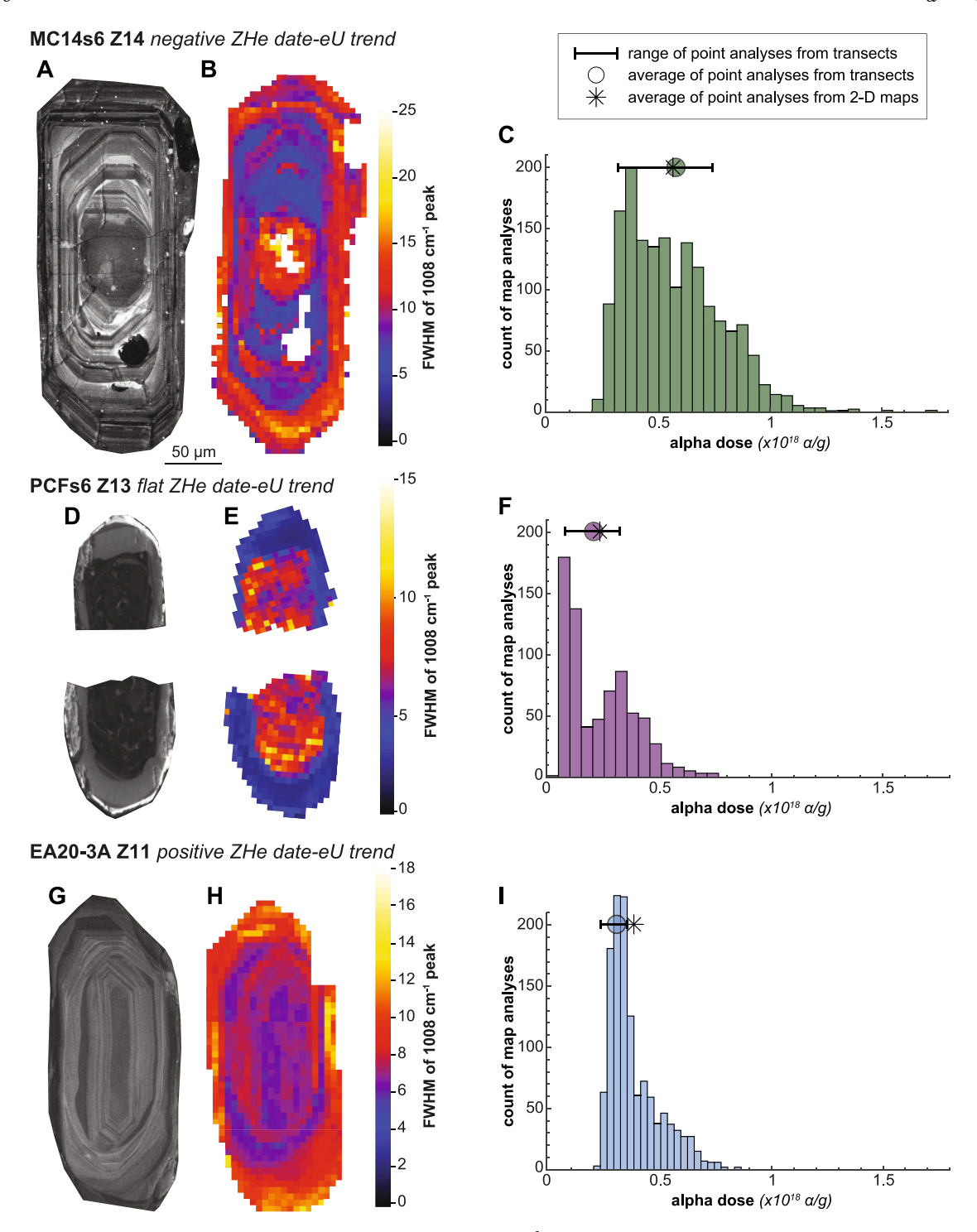


Fig. 5. (A, D, G) Cathodoluminesence map, (B, E, H) Raman map of FWHM of 1008 cm<sup>-1</sup> peak, and (C, F, I) histogram of alpha dose values calculated from 2-D map FWHM values for grains MC14s6 Z14, PCFs6 Z13, and EA20–3A Z11. Note different FWHM scales for B, E, and F. Star and circle on histograms are average alpha dose from all map analyses and average alpha dose from internal and external transects of six total spots, respectively. Horizontal bar denotes range of alpha dose values from transects.

Z6-Z10 in A12–8 have similar moderate visual metamictization and calculated alpha dose values (Figs. 1, 2D). In highly metamict zircon grains, it is challenging to assign ascending Z number among opaque crystals and the broad FWHM of the 1008 cm<sup>-1</sup> peak results in a maximum permissible alpha dose that further skews the alpha dose-Z number trend. For example, in A10–3, Z7-Z14 exhibit very high visual metamictization (Fig. 1) and individual Raman analyses from almost all grains have maximum alpha dose values (Fig. 2B). Similarly, Z10-Z13 in sample A10–42 are opaque and most of the grains yield individual alpha

dose analyses that are assigned the maximum values (Figs. 1, 2A). Thus, the natural characteristics of a given zircon grain population can impact Z number-effective radiation damage trends.

In addition, most of our zircon grains are zoned with respect to eU and effective radiation damage. Three-dimensional regions of different eU concentration in a zircon grain produce corresponding zones of variable effective radiation damage depending on the thermal history (e. g., Guenthner et al., 2013; Danišík et al., 2017). Damage zonation is visualized in our datasets in four complementary ways. First,

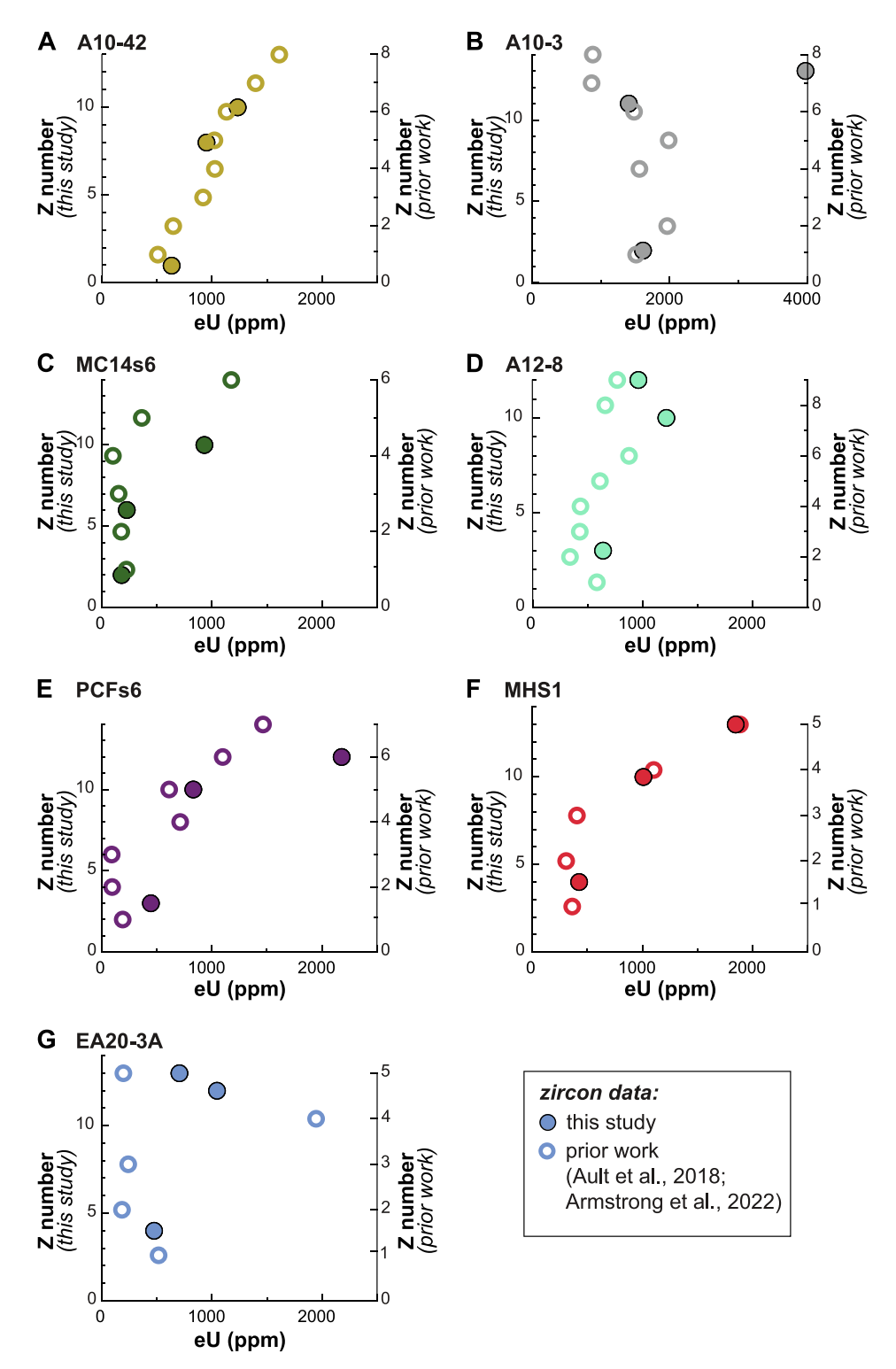


Fig. 6. Zircon grain Z number as a function of eU for this study (filled symbols) and prior work (open symbols; Ault et al., 2018; Armstrong et al., 2022). For this study, only three grains per sample have eU measurements.

stereoscopic images in plane polarized light reveal intragrain variability in visual metamictization (e.g., Z3 in sample A10–3). Second, zoning manifests as variable individual alpha dose values for each grain in Fig. 2, as well as divergent individual and average external and internal calculated alpha dose values in Figs. 3 and 4 (i.e., scatter around the 1:1 line). Third, zoning is observed in CL images (Figs. 5A, D, G, S7). Finally, 2-D Raman maps reveal that the three targeted grains are zoned (Fig. 5B, E, H).

Radiation damage zonation impacts visual metamictization-calculated alpha dose trends. In part, this reflects the comparison between a bulk assessment of damage (i.e., Z number) with multiple Raman point analyses from each grain. The relationship between these parameters is most impacted when grains are characterized by a high magnitude of damage zonation (i.e., samples A10-42 and A10-3). Zonation can cause scatter in samples characterized by overall positive trends between visual metamictization and calculated alpha dose. For

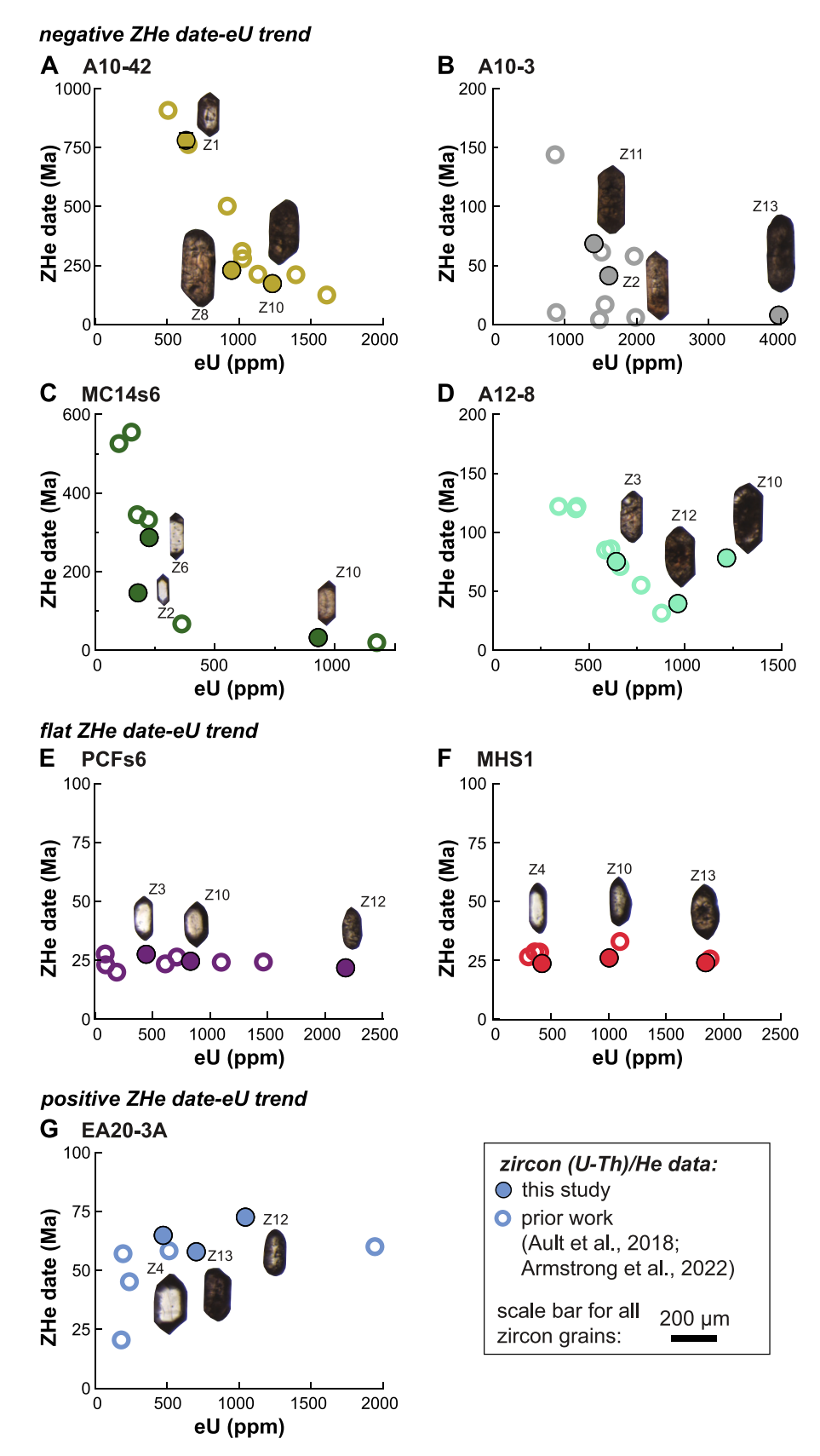


Fig. 7. Zircon (U-Th)/He (ZHe) date as a function of effective uranium (eU) for this study (filled symbols) and prior work (open symbols; Ault et al., 2018; Armstrong et al., 2022). Stereoscopic images of zircon grains analyzed in this study shown. Note x and y axis scales vary to highlight ZHe date-eU trends. 2 s error bars on ZHe dates hidden by data points.

example, Z13 in sample PCFs6 is characterized by a core-rim relationship, with a thick, CL-activated rim (Fig. 5D). This grain yields higher internal alpha dose values than external alpha dose measurements (Fig. 3E), consistent with the lower damage (i.e., lower FWHM) rim in the 2-D Raman map (Fig. 5E). In contrast, Z14 in this sample has similar internal and external calculated alpha dose values that plot near the 1:1 line (Fig. 3E) and subtle zoning in CL (Fig. S7). Sample MC14s6 Z14 has oscillatory zoning in CL (Fig. 5A), oscillatory FWHM values in the 2-D Raman map (Fig. 5B), and overlapping but scattered internal and external alpha dose values (Fig. 2C). Grain Z11 in sample EA20–3A exhibits oscillatory zoning in CL (Fig. 5G), oscillatory FWHM values in the 2-D Raman map (Fig. 5H), and diverging internal and external alpha dose values (Fig. 3G).

# 5.3. Relationships between effective radiation damage and visual metamictization across ZHe date-eU patterns

Our collective results allow us to connect zircon visual metamictization and effective radiation damage across ZHe date-eU trends to address outstanding questions from prior work (Ault et al., 2018; Moser et al., 2021) and assess potential limitations of this grain selection approach. Raman-calculated alpha dose increases with increasing Z number in at least one sample per type of ZHe date-eU trend (Fig. 2). Across similar ranges in intrasample eU produced by application of the visual metamictization grain selection approach, the magnitude of effective damage varies depending on the ZHe date-eU pattern reflecting the influence of a sample's thermal history on ZHe dates and accumulated and annealed damage through time.

The samples characterized by negative ZHe date-eU trends (A10-42, A10-3, MC14s6, A12-8) yield the overall highest calculated alpha dose values compared to samples characterized by flat or positive ZHe dateeU trends (Figs. 2, 4). This is not surprising given that zircon grains in these samples have Proterozoic and Archean crystallization ages (Table S1) and prior work suggests these samples spent sufficient time at temperature (depth) conditions where radiation damage (visual metamictization) can accumulate in grains as a function of eU (i.e., <225 °C; Garver and Kamp, 2002; Ault et al., 2018; Ricketts et al., 2021). The relationship between alpha dose and visual metamictization is most pronounced in sample MC14s6 (Fig. 2C), which is characterized by a demonstrable gradient in visual metamictization. In contrast, sample A12-8 with its similar level of visual metamictization across most grains exhibits a more limited increase in alpha dose (Fig. 2D). The relationship between alpha dose and Z number is less clear in A10-42 and A10-3 due to the preponderance of highly metamict and zoned grains (Figs. 1, 2, 3).

Sample EA20-3A, characterized by a positive ZHe date-eU trend, has a more subtle and scattered relationship between visual metamictization and Raman-calculated alpha dose than MC14s6 (Fig. 2G) for three reasons. First, a subset of EA20-3A grains exhibit a similar level of visual metamictization. Second, zircon grains in this sample are detrital and likely have Phanerozoic crystallization ages, although Proterozoic crystallization ages are possible (Ingersoll et al., 2013; Coffey et al., 2019). These grains experienced moderate reheating during at least one burial event resulting in He loss from the lowest eU grains to produce the observed positive ZHe date-eU trend (Armstrong et al., 2022). Third, EA20-3A grains have had less time for damage to accumulate compared to samples with negative ZHe date-eU patterns (cf. Fig. 9 in Guenthner et al., 2013). As a result, the overall magnitude of discoloration and opacity in grains from EA20-3A is lower than that of A12-8 and MC14s6 (Figs. 1, S2) and the magnitude of damage is lower (Fig. 4). Grains in sample EA20-3A still exhibit a range of visual metamictization despite their relatively young age, indicating the utility of the visual metamictization approach for samples beyond solely Precambrian grains.

Our new data demonstrate visual metamictization also reflects effective radiation damage in Paleoproterozoic samples characterized by uniform ZHe dates regardless of eU concentration. Prior studies speculated that samples PCFs6 and MHS1 experienced a thermal history

in which He was lost but radiation damage was not fully annealed, preserving the visually metamict appearance of some grains even though their ZHe dates are internally reproducible across a 2000 ppm spread in eU values (Ault et al., 2018; Moser et al., 2021). Raman spectroscopy data from PCFs6 and MHS1 zircons reveal increasing alpha dose with increasing Z number and eU (Figs. 2E, F, 6E, F), although damage in PCFs6 increases more than MHS1 over the same range of Z numbers. This not only adds support to our interpretation that visual metamictization tracks effective radiation damage regardless of ZHe date-eU trend, but also illustrates that the temperatures that He diffuses and radiation damage anneals in zircon are not the same (see Section 5.4).

Parent isotope zonation influences ZHe date-eU-visual metamictization relationships in multiple ways. Regardless of ZHe date-eU trend type, zonation introduces intrasample scatter in bulk ZHe dates owing to inaccurate alpha ejection correction factors associated with assuming a homogenous distribution of eU in standard (U-Th)/He date calculations (Reiners et al., 2004; Hourigan et al., 2005; Orme et al., 2015; Bargnesi et al., 2016). In addition, depending on the thermal history, spatially heterogeneous effective radiation damage influences He diffusion (Guenthner et al., 2013). For example, grain Z10 in sample A12–8 has the highest eU (1217 ppm) of all aliquots for this sample and also deviates from the overall negative ZHe date-eU trend (Fig. 5D). The ZHe date for this zircon is ~78 Ma, which is similar to the lower eU (642 ppm) grain Z3 with a  $\sim$  75 Ma ZHe date. Although we do not have CL imagery for Z10, in stereoscopic images it has a large, highly metamict core and a thin, less metamict rim (Fig. 1). Z10 may have an anomalously old ZHe date because the low damage rim is more retentive with respect to He (Fig. 5D). We note that fluid inclusions or vacancies that can trap He may also impact the ZHe date-eU-visual metamictization relationship in this and other samples (Danišík et al., 2017). Zonation effects are magnified in samples that experienced protracted thermal histories (i.e., negative ZHe date-eU trends); these samples have higher bulk damage (Fig. 2) and thus enhanced spatially variable damage (Fig. 4).

#### 5.4. Visual metamictization perspectives on damage annealing

Our results support preserved visual metamictization and measured damage persist through high temperatures and when grains are characterized by overall high damage. For example, samples PCFs6 and MHS1 experienced temperatures in excess of 600 °C prior to exhumation to upper crustal conditions (Jacobson et al., 2007; Moser et al., 2021). Persistent damage in these samples implies annealing requires higher temperatures than predicted by annealing kinetics as they are parameterized in the original ZRDAAM (Guenthner et al., 2013) or in a newer model implemented in Matlab (Guenthner, 2021) that uses the annealing kinetics of Ginster et al. (2019). ZRDAAM uses zircon fission track annealing as a proxy for overall damage annealing (Yamada et al., 2007). The Ginster et al. (2019) model is based on annealing experiments that quantified bulk radiation damage with the 1008 cm<sup>-1</sup> Raman band, similar to our characterization study. This model reveals bulk zircon damage requires higher temperatures to anneal than fission tracks. In addition, annealing may be damage-level dependent and highly damaged grains may never anneal (Ginster et al., 2019). Persistent visual metamictization and measured alpha dose in high Z numbers in samples like A10-42 and A10-3 support this.

At the same time, comparison of data from grains in different samples with the same eU content reveals that temperature-dependent annealing of radiation damage may manifest in some reduction of visual metamictization (i.e., increase in grain transparency). For example, zircon crystals from PCFs6 and MHS1 are not as visually metamict and have lower alpha dose for a similar range in eU measured in A12–8 zircon grains (Figs. 1, 2, 6), despite A12–8 zircon crystallizing a minimum of one hundred million years after MHS1 and PCFs6 (Table S1). The PCFs6 and MHS1 thermal history either did not allow for as much

damage accumulation or some damage did anneal, which decreased the opacity of these zircon grains in comparison to A12–8. Additional work characterizing color and opacity change in response to laboratory annealing is required to evaluate these temperature-sensitive textural changes.

#### 6. Conclusion and application to future studies

In this study, we revisit zircon mineral separates from samples reported in Ault et al. (2018) and Armstrong et al. (2022) to evaluate relationships between visual metamictization (Z number), effective damage calculated from Raman spectroscopy (alpha dose), and ZHe dates. Different analysts or the same analyst in different sessions selected zircon grains that encompass a similar range of visual metamictization and yield a similar range in eU concentration for each of these samples. New ZHe dates are consistent with previously reported ZHe date-eU patterns.

Raman spectroscopy data and calculated alpha dose, a proxy for effective radiation damage, reveal increasing visual metamictization generally corresponds to increasing effective damage for each type of date-eU trend. But the strength of this relationship varies from sample to sample. A clear positive relationship between visual metamictization and effective damage requires that grains within a sample exhibit observable variability in visual metamictization. Limited spread in metamictization in a given grain population and heterogeneous damage zonation mute and complicate these patterns. In general, samples characterized by a negative ZHe date-eU trend should yield the strongest positive relationship between visual metamictization and effective damage owing to their protracted thermal history that allows damage to accumulate, unless grains are strongly influenced by zoning. In our samples characterized by uniform ZHe dates regardless of eU value, increasing visual metamictization also corresponds to increasing alpha dose. Although these samples have Paleoproterozoic crystallization ages, they experienced a thermal history that caused comparatively recent complete He loss while preserving visual metamictization. This highlights that the temperature at which He diffuses but radiation damage anneals and visual metamictization is reversed are not the same, and that damage persists at higher temperatures than is currently parameterized in damage-diffusivity models.

We suggest that the visual metamictization should be integrated into existing workflows for selecting zircon grains for bulk ZHe thermochronometry analysis (Fig. 8). We build on concepts presented by Garver and Kamp (2002) as applied to fission track analyses and Ault et al. (2018) as applied to ZHe thermochronometry, and show that purposefully selecting grains that encompass the range of visual metamictization can yield a range in eU and ZHe dates depending on the thermal history the grains experienced. Our new work demonstrates that visual metamictization tracks not only eU but also effective radiation damage. We note that the available range of visual metamictization inherent in a sample, user bias, and U-Th zonation may influence the spectrum of grains that are selected, their assigned Z number, and the detailed relationships between visual metamictization, ZHe date, and eU. In addition, spatially heterogeneous U and Th concentrations, and thus radiation damage, can be observed in stereoscope particularly in moderately metamict grains, which can be leveraged or avoided when selecting zircon crystals for analyses. Building an intrasample spread in eU and effective damage is important for characterizing ZHe date-eUeffective damage patterns. Practitioners can then leverage these relationships in forward and inverse thermal history models to make more robust tectonic, erosional, and geologic interpretations.

#### **Declaration of competing interest**

The authors declare the following financial interests/personal relationships which may be considered as potential competing interests:

Emma Armstrong reports financial support was provided by National Science Foundation. Alexis Ault reports financial support was provided by National Science Foundation.

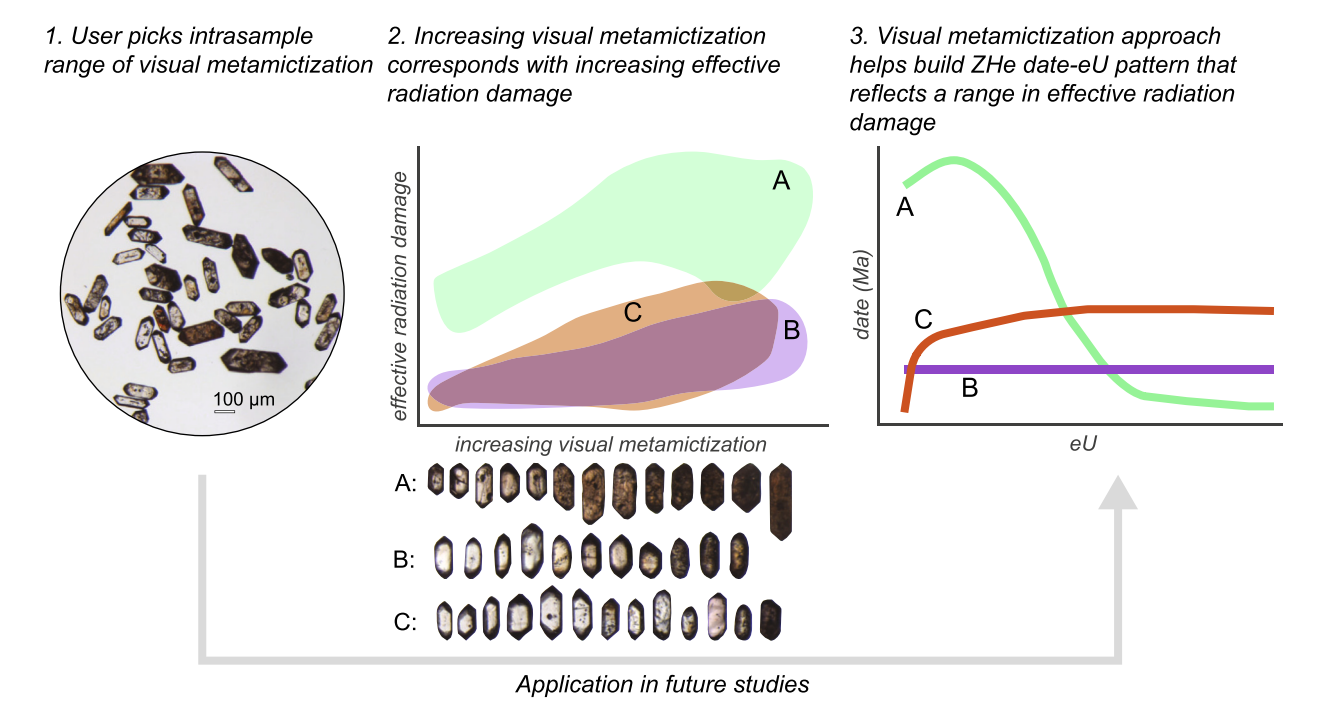


Fig. 8. Conceptual model of (1) zircon visual metamictization grain selection approach, (2) the relationship between effective radiation damage and visual metamictization for different ZHe date-eU patterns with targeted grains shown, and (3) different ZHe date-eU trends that develop from using this grain selection approach and resulting visual metamictization tracking effective radiation damage. Effective damage as a function of visual metamictization and ZHe date-eU patterns in (2) are outlined from data in Figs. 2 and 7.

#### Data availability

All information in the Supplemental Material and Table 1 is archived and freely available at figshare.com (https://doi.10.6084/m9.figshare.22259671) and ZHe analysis data are available at Geochron. org.

#### Acknowledgements

We thank Peter Reiners and Uttam Chowdhury (UA) for analytical assistance. Research was supported by NSF CAREER grant (EAR-1654628) to A. K. Ault, and an NSF Graduate Research Fellowship to E. M. Armstrong. We thank two anonymous reviewers and the Associate Editor Marco Fiorentini for comments that improved the clarity and organization of the manuscript.

### Appendix A. Supplementary data

Supplementary data to this article can be found online at https://doi.org/10.1016/j.chemgeo.2024.121949.

#### References

- Anderson, A.J., Hanchar, J.M., Hodges, K.V., van Soest, M.C., 2020. Mapping radiation damage zoning in zircon using Raman spectroscopy: implications for zircon chronology. Chem. Geol. 538, 119494 https://doi.org/10.1016/j. chemgeo.2020.119494.
- Armstrong, E., et al., 2022. A multi-proxy approach using zircon (U-Th)/He thermochronometry and biomarker thermal maturity to robustly capture earthquake temperature rise along the Punchbowl fault, California. Geochem. Geophys. Geosyst. 23 (4). 1–20. https://doi.org/10.1029/2021GC010291.
- Ault, A.K., Guenthner, W.R., Moser, A.C., Miller, G.H., Refsnider, K.A., 2018. Zircon grain selection reveals (de) coupled metamictization, radiation damage, and He diffusivity. Chem. Geol. 490, 1–12. https://doi.org/10.1016/j.chemgeo.2018.04.023.
- Ault, A.K., Gautheron, C., King, G.E., 2019. Innovations in (U–Th)/He, fission track, and trapped charge thermochronometry with applications to earthquakes, weathering, surface-mantle connections, and the growth and decay of mountains. Tectonics 38 (11), 3705–3739. https://doi.org/10.2029/2018TC005312.
- Bargnesi, E.A., Stockli, D.F., Hourigan, J.K., Hager, C., 2016. Improved accuracy of zircon (U-Th)/He ages by rectifying parent nuclide zonation with practical methods. Chem. Geol. 426, 158–169.
- Bethune, K.M., Scammel, R.J., 2003. Geology, petrology, and geochemistry of Archean rocks in the Eqe Bay Area, north-central Baffin Island: constraints on the depositional and tectonic history of the Mary River group of northeastern Rae Province. Can. J. Earth Sci. 40 (8) 1137–1167. https://doi.org/10.1139/e03-028
- Earth Sci. 40 (8), 1137–1167. https://doi.org/10.1139/e03-028.

  Coffey, K.T., Ingersoll, R.V., Schmitt, A.K., 2019. Stratigraphy, provenance, and tectonic significance of the Punchbowl block, San Gabriel Mountains, California, USA.

  Geosphere 15 (2) 479–501. https://doi.org/10.1130/GES02025.1
- Geosphere 15 (2), 479–501. https://doi.org/10.1130/GES02025.1.
  Cooperdock, E.H., Ketcham, R.A., Stockli, D.F., 2019. Resolving the effects of 2-D versus 3-D grain measurements on apatite (U–Th)/He age data and reproducibility. Geochronology 1 (1), 17–41.
- Corfu, F., Hanchar, J.M., Hoskin, P.W.O., Kinny, P., 2003. Atlas of zircon textures. Rev. Mineral. Geochem. 53, 468–500.
- Danišík, M., et al., 2017. Seeing is believing: visualization of He distribution in zircon and implications for thermal history reconstruction on single crystals. Sci. Adv. 3, e1601121.
- DeLucia, M.S., Guenthner, W.R., Marshak, S., Thomson, S.N., Ault, A.K., 2018. Thermochronology links denudation of the great unconformity surface to the supercontinent cycle and snowball Earth. Geology 46 (2), 167–170. https://doi.org/ 10.110/CCCCPT.
- Ewing, R.C., Meldrum, A., Wang, L., Weber, W.J., Rene Corrales, L., 2003. Radiation effects in zircon. Rev. Mineral. Geochem. 53 (1), 387–425. https://doi.org/10.2113/
- Flowers, R.M., Macdonald, F.A., Siddoway, C.S., Havranek, R., 2020. Diachronous development of great unconformities before Neoproterozoic snowball Earth. Proc. Natl. Acad. Sci. 117 (19), 10172–10180. https://doi.org/10.1073/ pnas.1913131117.
- Garver, J.I., Kamp, P.J.J., 2002. Integration of zircon color and zircon fission-track zonation patterns in orogenic belts: application to the Southern Alps, New Zealand. Tectonophysics 349 (1-4), 203–219. https://doi.org/10.1016/S0040-1951(02) 00054-9
- Gastil, R.G., DeLisle, M., Morgan, J., 1967. Some effects of progressive metamorphism on zircons. Geol. Soc. Am. Bull. 78, 879–906. https://doi.org/10.1130/0016-7606 (1967)78[879:SEOPMO]2.0.CO;2.
- Ginster, U., Reiners, P.W., Nasdala, L., Chanmuang, N.C., 2019. Annealing kinetics of radiation damage in zircon. Geochim. Cosmochim. Acta 249, 225–246. https://doi. org/10.1016/j.gca.2019.01.033.

- Guenthner, W.R., 2021. Implementation of an alpha damage annealing model for zircon (U-Th)/He thermochronology with comparison to a zircon fission track annealing model. Geochem. Geophys. Geosyst. 22 (2) https://doi.org/10.1029/2019GC008757 e2019GC008757.
- Guenthner, W.R., Reiners, P.W., Ketcham, R.A., Nasdala, L., Giester, G., 2013. Helium diffusion in natural zircon: radiation damage, anisotropy, and the interpretation of zircon (U-Th)/He thermochronology. Am. J. Sci. 313 (3), 145–198. https://doi.org/ 10.2475/03.2013.01.
- Guenthner, W.R., Reiners, P.W., Tian, Y., 2014. Interpreting date-eU correlations in zircon (U-Th)/He datasets: a case study from the Longmen Shan, China. Earth Planet. Sci. Lett. 403, 328–339. https://doi.org/10.1016/j.epsl.2014.06.050.
- Guenthner, W.R., Reiners, P.W., Chowdhury, U., 2016. Isotope dilution analysis of Ca and Ze in apatite and zircon (U-Th)/He chronometry. Geochem. Geophys. Geosyst. 17, 1623–1640. https://doi.org/10.1002/2016GC006311.
- Guenthner, W.R., Reiners, P.W., Drake, H., Tillberg, M., 2017. Zircon, titanite, and apatite (U-Th)/He ages and age-eU correlations from the Fennoscandian Shield, southern Sweden. Tectonics 36, 1254–1274. https://doi.org/10.1002/ 2017TC004525
- Hanchar, J., Miller, C., 1993. Zircon zonation patterns as revealed by cathodoluminescence and backscattered electron images: implications for interpretation of complex crustal histories. Chem. Geol. 110 (1–3), 1–13.
- Havranek, R.E., Flowers, R.M., 2022. Zircon (U-Th)/He data for the Colorado front range "fourteeners" and testing cryogenian exhumation of sub-great unconformity basement. Chem. Geol. 591, 120702 https://doi.org/10.1016/j.
- Holland, H.D., Gottfried, D., 1955. The effect of nuclear radiation on the structure of zircon. Acta Crystallogr. 8, 291–300. https://doi.org/10.1107/ S0365110X55000947.
- Hourigan, J.K., Reiners, P.W., Brandon, M.T., 2005. U-Th zonation-dependent alphaejection in (U-Th)/He chronometry. Geochim. Cosmochim. Acta 69 (13), 3349–3365. https://doi.org/10.1016/j.gca.2005.01.024.
- Hurley, P.M., 1952. Alpha ionization damage as a cause of low helium ratios. Trans. Am. Geophys. Union 33 (2), 174–183. https://doi.org/10.1029/TR033i002p00174.
- Ingersoll, R.V., Grove, M., Jacobson, C.E., Kimbrough, D.L., Hoyt, J.F., 2013. Detrital zircons indicate no drainage link between southern California rivers and the Colorado Plateau from mid-cretaceous through Pliocene. Geology 41 (3), 311–314. https://doi.org/10.1130/G33807.1.
- Jackson, G.D., Hunt, P.A., Loveridge, W.D., Parrish, R.R., 1990. Reconnaissance geochronology of Baffin Island, N.W.T. Geol, Surv. Can. Pap. 89 (2), 123–148.
- Jacobson, C.E., Grove, M., Vucic, A., Pedrick, J.N., Ebert, K.A., 2007. Exhumation of the Orocopia Schist and associated rocks of southeastern California: relative roles of erosion, synsubduction tectonic denudation, and middle Cenozoic extension. Geol. Soc. Am. Spec. Pap. 419, 1–37. https://doi.org/10.1130/2007.2419(01).
- Johnson, J.E., Flowers, R.M., Baird, G.B., Mahan, K.H., 2017. "Inverted" zircon and apatite (U-Th)/He dates from the Front Range, Colorado: high-damage zircon as a low-temperature (< 50° C) thermochronometer. Earth Planet. Sci. Lett. 466, 80–90. https://doi.org/10.1016/j.epsl.2017.03.002.</p>
- Kempe, U., Trinkler, M., Pöppl, A., Himcinschi, C., 2016. Coloration of natural zircon. Can. Mineral. 54 (3), 635–660.
- Ketcham, R.A., 2005. Forward and inverse modeling of low-temperature thermochronometry data. Rev. Mineral. Geochem. 58 (1), 275–314.
- Ketcham, R.A., Guenthner, W.R., Reiners, P.W., 2013. Geometric analysis of radiation damage connectivity in zircon and its implications for He diffusion. Am. Mineral. 98 (2–3), 350–360. https://doi.org/10.2138/am.2013.4249.
- Kirby, E., Karlstrom, K.E., Andronicos, C.L., Dallmeyer, R.D., 1995. Tectonic setting of the Sandia pluton: an orogenic 1.4 Ga granite in New Mexico. Tectonics 14 (1), 185–201. https://doi.org/10.1029/94TC02699.
- Machado, J.P., Jelinek, A.R., Stephenson, R., O'Sullivan, P., 2021. Thermochronology of South America passive margin between Uruguay and southern Brazil: a lengthy and complex cooling history based on (U–Th)/He and fission tracks. J. S. Am. Earth Sci. 106, 103019 https://doi.org/10.1016/j.jsames.2020.103019.
- Marsellos, A.E., Garver, J.I., 2010. Radiation damage and uranium concentration in zircon as assessed by Raman spectroscopy and neutron irradiation. Am. Mineral. 95 (8–9), 1192–1201. https://doi.org/10.2138/am.2010.3264.
- McDermott, R.G., Ault, A.K., Caine, J.S., Thomson, S.N., 2019. Thermotectonic history of the Kluane Ranges and evolution of the eastern Denali fault zone in southwestern Yukon, Canada. Tectonics. https://doi.org/10.1029/2019TC005545.
- McMillan, M., Boone, S., Kohn, B., Gleadow, A., Chindandali, P., 2022. Development of the Nyika Plateau, Malawi: a long lived paleo-surface or a contemporary feature of the East African rift? Geochem. Geophys. Geosyst. 23 (8) e2022GC010390.
- Moser, A., Ault, A., Stearns, M., Evans, J., Guenthner, W., 2021. Late oligocene–early miocene detachment faulting in crystalline basement, Mecca Hills, CA, documented with zircon (U–Th)/He date-eU-visual radiation damage patterns. Tectonics 40 (9), 1–24. https://doi.org/10.1029/2021TC006809.
- Nasdala, L., Irmer, G., Wolf, D., 1995. The degree of metamictization in zircon: a Raman spectroscopic study. Eur. J. Mineral. 7 (3), 471–478. https://doi.org/10.1127/ejm/ 7/3/0471
- Nasdala, L., et al., 2001. Metamictisation of natural zircon: accumulation versus thermal annealing of radioactivity-induced damage. Contrib. Mineral. Petrol. 141 (2), 125–144. https://doi.org/10.1007/s004100000235.
- Nasdala, L., et al., 2003. Spectroscopic methods applied to zircon. Rev. Mineral. Geochem. 53 (1), 427–467. https://doi.org/10.2113/0530427.
- Orme, D.A., Reiners, P.W., Hourigan, J.K., Carrapa, B., 2015. Effects of inherited cores and magmatic overgrowths on zircon (U-Th)/He ages and age-eU trends from Greater Himalayan sequence rocks, Mount Everest region, Tibet. Geochem. Geophys. Geosyst. 16, 2499–2507. https://doi.org/10.1002/2015GC005818.

- Orme, D.A., Guenthner, W.R., Laskowski, A.K., Reiners, P.W., 2016. Long-term tectonothermal history of Laramide basement from zircon-He age-eU correlations. Earth Planet. Sci. Lett. 453, 119–130. https://doi.org/10.1016/j.epsl.2016.07.046.
- Peak, B., Flowers, R., Macdonald, F., Cottle, J., 2021. Zircon (U-Th)/He thermochronology reveals pre-great unconformity paleotopography in the Grand Canyon region, USA. Geology 49 (12), 1462–1466. https://doi.org/10.1130/ G49116.1.
- Powell, J., Schneider, D., Stockli, D.F., Fallas, K., 2016. Zircon (U-Th)/He thermochronology of Neoproterozoic strata from the Mackenzie Mountains, Canada: implications for the Phanerozoic exhumation and deformation history of the northern Canadian Cordillera. Tectonics 35 (3), 663–689. https://doi.org/10.1002/ 2015TC003989.
- Premo, W.R., Fanning, C.M., 2000. SHRIMP U-Pb zircon ages for Big Creek gneiss, Wyoming and Boulder Creek batholith, Colorado: implications for timing of Paleoproterozoic accretion of the northern Colorado province. Rocky Mt. Geol. 35 (1), 31–50. https://doi.org/10.2113/35.1.31.
- Rayner, N.M., Sanborn-Barrie, M., Young, M.D., Whalen, J.B., 2012. U-Pb ages of Archean basement and Paleoproterozoic plutonic rocks southern Cumberland Peninsula, eastern Baffin Island, Nunavut. Geol. Surv. Can. Curr. Res. 2012 (8), 1–24.
- Reiners, P.W., 2005. Zircon (U-Th)/He thermochronometry. Rev. Mineral. Geochem. 58 (1), 151–179. https://doi.org/10.2138/rmg.2005.58.6.
- Reiners, P.W., Spell, T.L., Nicolescu, S., Zanetti, K.A., 2004. Zircon (U-Th)/He thermochronometry: he diffusion and comparisons with 40Ar/39Ar dating. Geochim. Cosmochim. Acta 68 (8), 1857–1887. https://doi.org/10.1016/j.gca.2003.10.021.

- Ricketts, J., Amato, J., Gavel, M., 2021. The origin and tectonic significance of the Basin and Range–Rio Grande rift boundary in southern New Mexico, USA. GSA Today 31 (10), 4–10. https://doi.org/10.1130/GSATG509A.1.
- Ronemus, C.B., Orme, D.A., Guenthner, W.R., Cox, S.E., Kussmaul, C.A., 2023. Orogens of Big Sky Country: reconstructing the deep-time tectonothermal history of the Beartooth Mountains, Montana and Wyoming, USA. Tectonics 42 (1) e2022TC007541.
- Shuster, D.L., Farley, K.A., 2009. The influence of artificial radiation damage and thermal annealing on helium diffusion kinetics in apatite. Geochim. Cosmochim. Acta 73, 183–196. https://doi.org/10.1016/j.gca.2008.10.013.
- Thurston, O.G., et al., 2022. Zircon (U-Th)/He thermochronology of Grand Canyon resolves 1250 Ma unroofing at the great unconformity and < 20 Ma canyon carving. Geology 50 (2), 222–226. https://doi.org/10.1130/G48699.1.
- Váczi, T., Nasdala, L., 2017. Electron-beam-induced annealing of natural zircon: a Raman spectroscopic study. Phys. Chem. Miner. 44 (6), 389–401. https://doi.org/10.1007/ s00269-016-0866-x.
- Woodhead, J.A., Rossman, G.R., Silver, L.T., 1991. The metamictization of zircon: radiation dose-dependent structural characteristics. Am. Mineral. 76, 74–82.
- Yamada, R., Murakami, M., Tagami, T., 2007. Statistical modelling of annealing kinetics of fission tracks in zircon; reassessment of laboratory experiments. Chem. Geol. 236 (1–2), 75–91. https://doi.org/10.1016/j.chemgeo.2006.09.002.
- Zhang, M., et al., 2000. Annealing of-decay damage in zircon: a Raman spectroscopic study. J. Phys. Condens. Matter 12 (13), 3131. https://doi.org/10.1088/0953-8984/ 12/13/321.